



**HAL**  
open science

**Facies and architecture of the SCIC formation  
(Schisto-Calcaire Group), Republic of the Congo, in the  
Niari-Nyanga and Comba subbasins of the  
neoproterozoic west Congo basin after the marinoan  
glaciation event**

Anna Perla Ackouala Mfere, Franck Delpomdor, Jean-Noël Proust, Florent  
Boudzoumou, Yannick y Callec, Alain Pr at

► **To cite this version:**

Anna Perla Ackouala Mfere, Franck Delpomdor, Jean-No l Proust, Florent Boudzoumou, Yannick y Callec, et al.. Facies and architecture of the SCIC formation (Schisto-Calcaire Group), Republic of the Congo, in the Niari-Nyanga and Comba subbasins of the neoproterozoic west Congo basin after the marinoan glaciation event. *Journal of African Earth Sciences*, 2020, 166, pp.103776. 10.1016/j.jafrearsci.2020.103776 . insu-02497974

**HAL Id: insu-02497974**

**<https://insu.hal.science/insu-02497974>**

Submitted on 4 Mar 2020

**HAL** is a multi-disciplinary open access archive for the deposit and dissemination of scientific research documents, whether they are published or not. The documents may come from teaching and research institutions in France or abroad, or from public or private research centers.

L'archive ouverte pluridisciplinaire **HAL**, est destin e au d p t et   la diffusion de documents scientifiques de niveau recherche, publi s ou non,  manant des  tablissements d'enseignement et de recherche fran ais ou  trangers, des laboratoires publics ou priv s.



Distributed under a Creative Commons Attribution - NonCommercial - NoDerivatives 4.0  
International License

# Journal Pre-proof

Facies and architecture of the SC1c formation (Schisto-Calcaire Group), Republic of the Congo, in the Niari-Nyanga and Comba subbasins of the neoproterozoic west Congo basin after the marinoan glaciation event

Anna Perla Ackouala Mfere, Franck Delpomdor, Jean-Noël Proust, Florent Boudzoumou, Yannick Callec, Alain Pr at

PII: S1464-343X(20)30027-3

DOI: <https://doi.org/10.1016/j.jafrearsci.2020.103776>

Reference: AES 103776

To appear in: *Journal of African Earth Sciences*

Received Date: 18 December 2018

Revised Date: 24 January 2020

Accepted Date: 24 January 2020

Please cite this article as: Mfere, A.P.A., Delpomdor, F., Proust, Jean.-No ., Boudzoumou, F., Callec, Y., Pr at, A., Facies and architecture of the SC1c formation (Schisto-Calcaire Group), Republic of the Congo, in the Niari-Nyanga and Comba subbasins of the neoproterozoic west Congo basin after the marinoan glaciation event, *Journal of African Earth Sciences* (2020), doi: <https://doi.org/10.1016/j.jafrearsci.2020.103776>.

This is a PDF file of an article that has undergone enhancements after acceptance, such as the addition of a cover page and metadata, and formatting for readability, but it is not yet the definitive version of record. This version will undergo additional copyediting, typesetting and review before it is published in its final form, but we are providing this version to give early visibility of the article. Please note that, during the production process, errors may be discovered which could affect the content, and all legal disclaimers that apply to the journal pertain.

  2020 Published by Elsevier Ltd.



1 **Facies and architecture of the SCI<sub>c</sub> Formation (Schisto-Calcaire Group), Republic of**  
2 **the Congo, in the Niari-Nyanga and Comba subbasins of the Neoproterozoic West**  
3 **Congo Basin after the Marinoan glaciation event**

4

5 **Authors:**

6 Anna Perla Ackouala Mfere<sup>1,2\*</sup>, Franck Delpomdor<sup>3</sup>, Jean-Noël Proust<sup>4</sup>, Florent Boudzoumou<sup>2</sup>,  
7 Yannick Callec<sup>5</sup>, Alain Pr  at<sup>1</sup>

8

9 **Affiliations:**

10 <sup>1</sup>*Universit   Libre de Bruxelles, Department of Earth Sciences and Environmental Sciences, 50 av. FD*  
11 *Roosevelt, B-1050, Brussels, Belgium, Corresponding author: ackouala8@yahoo.fr*

12 <sup>2</sup>*Universit   Marien Ngouabi, D  partement de G  ologie BP69, Brazzaville, People's Republic of the Congo*

13 <sup>3</sup>*Illinois State Geological Survey, University of Illinois at Urbana-Champaign, 615 E. Peabody Dr, US-61820,*  
14 *Champaign, IL, USA*

15 <sup>4</sup>*Univ Rennes, CNRS, UMR6118 Geosciences, 35000 Rennes, France*

16 <sup>5</sup>*Bureau de Recherches G  ologiques et Mini  res, 3 av. Claude Guillemin, BP 36009, F-45060 Orl  ans,*  
17 *C  dex2, France*

18

19 **Keywords:** Neoproterozoic, West Congolian Supergroup, Facies, Sequence stratigraphy, Basin  
20 evolution

21

22 **Abstract**

23 The Neoproterozoic Schisto-Calcaire Group (630 to ca. 580 Ma) was deposited on an extensive  
24 carbonate shelf in the margin of the Congo Craton in the Niari-Nyanga and Comba subbasins (Gabon  
25 and Republic of the Congo). It consists of three carbonate-dominated subgroups (SCI to SCIII, up to  
26 1300 m-thick) recording relative sea-level changes. The SCI<sub>c</sub> Formation, at the upper part of the SCI  
27 Subgroup, is a carbonate succession of meter-scale shallowing-upward cycles, composed of a standard  
28 sequence of 7 facies grouped in 5 facies associations recording the evolution of a marine ramp from  
29 distal carbonate muds and giant stromatolitic bioherms (F1-F2) and extensive ooid shoals (F3), to

30 proximal settings submitted to evaporation near a sabkha (F7). Fifth-order 'meter-scale' (or  
31 elementary parasequences) packages are grouped into fourth-order sequences (parasequence sets),  
32 which are not correlative in the whole basin. Two categories of fifth-order elementary parasequences  
33 are recognized, on the basis of physical bounding surfaces: (i) subtidal cycles bounded by marine  
34 flooding surfaces across which subfacies deepen; and (ii) peritidal cycles bounded by subaerial  
35 exposure surfaces. These cycles are the result of the interplay of relative sea-level changes due to  
36 eustatic variations related to periodic extensional tectonic events affecting the whole basin. The Niari-  
37 Nyanga and Comba subbasins experienced basin tectonics in the general context of the rifting of  
38 Rodinia creating changes of relative sea-level in the different parts of the shelf. The SCI<sub>c</sub> cycles are  
39 enclosed into a third-order sequence with two major transgressive-regressive phases, related to the  
40 deposition of the SCI Subgroup. The most typical sedimentologic feature of the SCI<sub>c</sub> Formation is the  
41 deposition of giant stromatolitic bioherms (stacked up to 20 m) topped by ooid shoals (up to 75 meters  
42 thick) deposited during high systems tract prograding and forced regressive systems tract phases that  
43 ended with a lowstand systems tract phase with evaporitic and karstic conditions at the top of the SCI<sub>c</sub>  
44 Formation. The elementary parasequences and parasequence sets are probably the result of the  
45 migration of lateral environments related to the variation of the energy in relation to tectonic setting.  
46 As a result, a regional sea-level increase is for the first time highlighted in transgressive systems tract  
47 phase (composed of microbial induced sedimentary structures Facies) in the lower part of the SCI<sub>c</sub>  
48 Formation. The third-order succession can be followed more than 100 km in the Republic of the  
49 Congo and several hundred meters from South of Gabon to the Lower Congo in the Democratic  
50 Republic of the Congo. Tentative detailed sequence stratigraphy correlations between both Congo's  
51 highlight the role of tectonics affecting both areas.

52

53 **1. Introduction**

54 The Neoproterozoic Era (~1000-540 Ma) was marked by several catastrophic Snowball Earth-type ice  
55 ages involving short-lived global climate and eustatic events (Kirchvink, 1992; Hoffman et al., 1998;  
56 Hoffman and Schrag, 2002). At least three long-live Neoproterozoic glacioeras (~715-660 Ma  
57 Sturtian, ~655-635 Ma Marinoan, and ~583-581 Ma Gaskiers events were widely identified (Young,  
58 1995; Wang and Li, 2003; Allen et al., 2004; Deynoux et al., 2006; Hoffman and Li, 2009; Hoffman et  
59 al., 2017). Each event was marked by the deposition of diamictites, widely distributed on all  
60 continents. The diamictites are commonly overlain in a sharp contact by a cap carbonate unit,  
61 interpreted as the result of a sudden switch back to a greenhouse (Hoffman and Schrag, 2002) climate  
62 related to increase of atmospheric carbon dioxide due to volcanic degassing (Hoffman and Schrag,  
63 2002). This latter event caused a rapid post-glacial marine transgression, and the turning on of the  
64 carbonate factory.

65 However, other works have cautioned that diamictites are not unambiguous glacial indicators, but  
66 could represent tectonostratigraphic successions formed in tectonically-active rift basins as Rodinia  
67 broke apart, thereby demanding caution in directly inferring glacially controlled climatic and eustatic  
68 interpretations from such successions (Direen and Jago, 2008; Eyles and Januszczak, 2004; Arnaud  
69 and Eyles, 2006; Carto and Eyles, 2012; Delpomdor et al., 2016). In western-central Africa, recent  
70 publications have argued that the post-Marinoan carbonate successions record a marine transgression,  
71 interconnected with diachronous and regional tectonic processes related to the onset of the pre-  
72 collisional magmatic arc in the Araçuaí-West Congo Orogen, dated around 630 Ma, with an orogenic  
73 climax around 585-560 Ma (Delpomdor et al., 2016, 2018, 2019).

74 The aim of our paper is to contribute to the debate on the deposition of carbonate successions in  
75 western-central Africa, recording a marine transgression after the Marinoan glaciation event. We  
76 propose (1) to re-interpret the deposition of the SCI<sub>c</sub> Formation in the Niari-Nyanga and Comba  
77 subbasins of the Neoproterozoic West Congo Basin (NWCB), located in the Republic of the Congo,  
78 and (2) to describe the vertical thickness variations in the cycles and their organization into different  
79 sequence orders as a result of tectonic and eustatic mechanisms. A particular interest concerns the  
80 hummocky cross-stratification or « HCS » in the oolitic shoals, which is reported for the first time in  
81 this stratigraphic unit. It should also be noted that the oolitic shoals are recently intensively used by  
82 the cement industry.

83

## 84 **2. Geological Setting**

85 The research area concerns exposures along 1,300 km of the western margin of the Congo Craton,  
86 from southwestern Gabon across the Republic of the Congo (RC) to the western part of the  
87 Democratic Republic of the Congo (DRC) to northern Angola (Fig. 1). The Pan-African West Congo  
88 Belt (WCB) is part of the Araçuaí-West Congo Orogen (AWCO) formed during the Gondwanaland  
89 amalgamation (ca. 550 Ma; Pedrosa-Soares et al., 2008). In RC, the WCB is subdivided into the  
90 aulacogen foreland and the Mayombe thrust-and-fold belt domains, which differ in deformation style  
91 and metamorphic grade. The foreland domain is composed of weakly to unmetamorphosed rocks  
92 unlike those of the thrust-and-fold belt domain. The WCB comprises several Neoproterozoic  
93 sedimentary subbasins (Tait et al., 2011; Delpomdor and Pr eat, 2013; Pr eat et al., 2011, 2018), here  
94 unified as the NWCB, which is now divided from north to south into the Niari-Nyanga, Comba,  
95 Lower Congo and North Angola subbasins (Fig. 1). The Niari-Nyanga and Comba subbasins in RC

96 are filled with volcano-sedimentary successions of the West Congolian Supergroup (WCS) (Dadet,  
97 1969; Alvarez and Maurin, 1991; Thiéblemont et al., 2009; Charles et al., 2015; Affaton et al., 2016;  
98 Préat et al., 2018). In RC, the lithostratigraphic terminology of the WCS has been recently modified  
99 by Charles et al. (2015) with, from base to top: (i) the rift-related volcano-sedimentary Sounda Group,  
100 correlated to the ~1000-930 Ma Nzadi and ~920-910 Ma Tshela/Senke Banza groups (including the  
101 Inga-Lufu- and Gangila-type bimodal magmatism) in DRC (Baudet et al., 2013), (ii) the passive-  
102 margin Mayombe Group, stratigraphic equivalent to the Sansikwa and Haut-Shiloango subgroups in  
103 DRC, (iii) the Niari Group formerly called the “Upper Diamictite”, (iv) the shallow marine Schisto-  
104 Calcaire Group, stratigraphic equivalent to the Lukala Subgroup in DRC, including a carbonate outer  
105 shelf with nearshore barriers and evaporitic lagoons, and (v) the late-orogenic Mpioka Group (Fig. 2).  
106 The Sounda Group is subdivided into the Nemba, Kakamoéka and Mvouti subgroups; the Mayombe  
107 Group includes the Mossouva, Lower Diamictite and Louila/Bouenza subgroups; the Schisto-Calcaire  
108 Group comprises the SCI, SCII and SCIII subgroups (Dadet, 1969; Alvarez and Maurin, 1991;  
109 Alvarez, 1995; Préat et al., 2018; Fig. 2).

110

### 111 **3. Geochronology**

112 The absolute age of the WCB is relatively well constrained. In DRC, the Sansikwa Subgroup, a  
113 stratigraphic equivalent to the Mossouva Subgroup of the Mayombe Group in RC, is younger than  
114 920-910 Ma (Tack et al., 2001). The Sansikwa Subgroup is intruded by the Sumbi-type dolerite feeder  
115 sills and dykes (De Paepe et al., 1975; Kampunzu et al., 1991). U-Pb determinations on baddeleyite  
116 single-grains from a dolerite sill yielded a crystallization age of  $694 \pm 4$  Ma (Straathof, 2011), an age  
117 younger than the formerly accepted Sturtian age. The Upper Diamictite Formation in DRC

118 (stratigraphic equivalent with the Niari Group in RC) is interlayered with basalts of tholeiitic affinity  
119 including the Kimbundu pillows and hyaloclastic breccias. In Gabon, zircons from a tuff in the  
120 metasedimentary Louila/Bouenza Subgroup yielded a U-Pb SHRIMP age of  $\leq 713 \pm 49$  Ma  
121 (Thiéblemont et al., 2009). Detrital zircon geochronology and provenance analysis of the Lower  
122 Diamictite Formation from DRC gave a maximum depositional age of  $\sim 700$  Ma (Muanza-Kant et al.,  
123 2016) constraining the episodic extensional activity recorded on the present-day African side of the  
124 AWCO. Detrital U-Pb single-zircon analysis from the basal contact of the upper formation of the  
125 Haut-Shiloango Subgroup in DRC, stratigraphically equivalent with the Louila/Bouenza Subgroup,  
126 points to a maximum depositional age of  $\sim 650$  Ma (Frimmel et al., 2006). Carbonates of the  
127 uppermost Haut-Shiloango Subgroup were probably deposited around 645 Ma, according to near-  
128 primary  $^{87}\text{Sr}/^{86}\text{Sr}$  ratios which are similar to carbonates deposited worldwide during this time interval  
129 (Frimmel et al., 2006; Poidevin, 2007). Similarly, carbonates of the CII unit of the Lukala Subgroup in  
130 DRC, stratigraphic equivalent with the SCII Schisto-Calcaire Group, were deposited around  $\sim 575$  Ma  
131 (Poidevin, 2007). Regional metamorphism of the WCB is constrained by an Ar-Ar age of  $566 \pm 42$  Ma  
132 (Frimmel et al., 2006) in good agreement with the  $\sim 585$ - $560$  Ma orogenic climax of the AWCO in  
133 Brazil (Pedrosa-Soares et al., 2011). Late Pan African tectonics are constrained by an Ar-Ar age of  
134  $524.6 \pm 4.6$  Ma on riebeckite in quartz vein in DRC (Tack et al., 2018) and an K-Ar age of  $499 \pm 19$   
135 Ma on illite crystallinity analysis from micas in the Mpioka Group (Fullgraf et al., 2015), that is  
136 coeval with 540-490 Ma ages obtained in Angola (Monié et al., 2012).

137 The SCI<sub>c</sub> has never been dated but is younger than the Niari Group that is overlain by the cap  
138 carbonates (SCI<sub>a</sub>), and is older than the carbonates of the SCII Subgroup of the Schisto-Calcaire  
139 Group (Fig. 2).

140

#### 141 **4. Methodology**

142 Twenty-seven stratigraphic sections were selected in the SCI<sub>c</sub> Formation from outcrops along roads,  
143 rivers and in the savanna in two key areas of the Niari-Nyanga and Comba subbasins of the NWCB  
144 (Fig. 3). The thinnest section is 2 meter-thick and the thickest is 57 meter-thick. Since the sections  
145 have been logged and described close to each other, sometimes in places without localities, it has not  
146 been possible to name them systematically according to the geographical locations. The 27 sections  
147 are named from B to Y (Ackouala Mfere, 2017) with also MAD8016, MAD8018 and MAD8019. The  
148 sections A and E belonging to the SCI<sub>b</sub> siltstones (Table 1) are not considered here, sections G and  
149 MAD8018 are located in active quarries (Sonocc at Loutété), section MAD1016 is located in Bitoto,  
150 section MAD8017 is located in an active quarry (Saris quarry, near Nkayi), and section MAD8019 is  
151 located near the locality of Zanzo (Fig. 3). The coordinates of the outcrops are summarized in Table 1.  
152 Up to 500 samples were collected for petrography and thin section analysis in order to describe facies  
153 associations. The carbonate classification terminologies of Dunham (1962), Embry and Klovan  
154 (1972), Sibley and Gregg (1987) were employed for the description of components, matrix and  
155 cements. The non-skeletal grains (ooids, intraclasts, peloids, aggregate grains, vadoids), sedimentary  
156 textures and structures were systematically quantified.

157

#### 158 **5. Facies association and depositional model**

159 The carbonates of the Schisto-Calcaire Group (SCI, SCII and SCIII Subgroups) were described by  
160 Pr  at et al. (2018). In this paper, we focus on the SCI<sub>c</sub> Formation that we describe and interpret in  
161 terms of depositional environments and sequences.

162 The SCI<sub>c</sub> succession contains five facies associations (FA1 to FA5) that are composed of seven facies  
163 (F1 to F7) defined by their lithologies, sedimentary structures, textures, fossil contents (microbial  
164 mats) and interpreted as deposited in different depositional environments. Facies 3 (F3) is divided into  
165 4 sub-types (F3a,b,c,d) due to the presence of ooids in the mentioned sub-types. These largely marine  
166 facies associations are described from the deepest to the shallowest settings and are summarized in  
167 Table 2. In this paper, ramp terminology was adopted from Burchette and Wright (1992) with (1) the  
168 outer-ramp below the storm wave base (SWB) in the offshore; (2) the mid-ramp between the SWB  
169 and the fair-weather wave base (FWWB) in the shoreface transition and (3) the inner-ramp above the  
170 FWWB including either high energy shoreface environments and back-shoal infratidal to supratidal  
171 environments (e.g., muddy lagoon, tidal flats, swamps) in the backshore.

172

### 173 ***Outer-ramp***

#### 174 *5.1. Facies association 1 (FA1)*

##### 175 Description

176 FA1 is represented by homogeneous clayey and laminar silty mudstone (F1) (Figs. 4A,C). The  
177 laminae consist of a subhorizontal, slightly undulating, alternation of light and darker layers of clayey  
178 carbonate siltstones and microbial dome-like (< 0.5 mm) or microlenticular (up to 2.5 mm) mudstones  
179 respectively (Figs. 4A-C).

180

##### 181 Interpretation

182 FA1 represents Microbial Induced Sedimentary Structures (MISS; *sensu* Noffke, 2010). The absence  
183 of ripple marks, hummocky cross-stratification (HCS), erosional remnants, mat chips, mat curls, true

184 fenestral fabrics, desiccation cracks and gas domes suggests a quiet and deep environment (40-60 m?)  
185 in the photic zone. The environment is typical of the offshore below SWB as for example on the  
186 Ordovician continental shelf of the Montagne Noire, France (Noffke, 2000).

187

## 188 ***Mid-Ramp***

### 189 *5.2. Facies association 2 (FA2)*

190 FA2 includes giant reefal stromatolites with stromatoclast floatstones (F2) and ooid  
191 grainstones (F3a with HCS).

192

#### 193 Description

194 F2 displays a variety of domes, columns and cone-shaped morphologies forming bioherms  
195 and/or biostromes (Figs. 5A-B and D). Reefs, ranging in sizes from 1 m up to 10 m, are  
196 exposed as isolated bodies or stacked in large complexes. Narrow inter-reef areas between the  
197 domes, and more commonly between the columns, are filled with stromatoclast floatstones  
198 with centimetric-sized and elongated fragments or breccias. F3a consists of grey colored  
199 oolite grainstones/packstones overlying F2. HCS with gently curved and low angle cross-  
200 laminations ( $< 10^\circ$ ) and swaley cross-stratifications (SCS) are associated with F3a (Figs. 6D-  
201 G). The oolites, ranging between 400  $\mu\text{m}$  and 650  $\mu\text{m}$  in diameter, are spherical, concentric or  
202 composite. Monocrystalline calcite or rosettes of former sulphate minerals often replace the  
203 nuclei.

#### 204 Interpretation

205 The giant dome- and cone-shaped stromatolites formed subaqueously in mid-ramp settings  
206 (Kromkamp et al., 2007; Perkins et al., 2007). Stromatoclasts suggest wave- and storm-  
207 dominated environments. F2 is locally interstratified and overlain by cross-stratified oolite  
208 grainstones of facies 3a (see below, Fig. 6H). HCS in the oolite grainstones (details in section  
209 6.2.) confirms sedimentation between the SWB and the FWWB. Oolites originally formed in  
210 shallow water more likely around 2 m deep (Keith and Zuppann, 1993) have been later  
211 removed from inner-ramp to the mid-ramp by wave action. Concentrically laminated oolites  
212 attest high-energy shoals. HCS are the result of storm action (Walker and Flint, 1992) in the  
213 shoreface transition region between SWB and FWWB ( Pedersen, 1985; Bose and Chaudhuri,  
214 1990).

215

## 216 ***Inner-ramp***

### 217 *5.3. Facies association 3 (FA3)*

218 FA3 includes oolite grainstones/packstones (F3a without HCS), floatstones/packstones (F3b) and  
219 (dolo)wackestones/(dolo)packstones-grainstones (F3c).

220

#### 221 Description

222 F3a consists of oolitic grainstones/packstones (Fig. 7A) overlying or interfering with the bioherms. F3  
223 shows planar stratifications, low-angle to tabular cross-beddings, asymmetrical current ripples and  
224 herringbone cross-beddings (Figs. 6A-B). The oolites are commonly spherical and concentric,  
225 between 400 µm and 650 µm in diameter, associated with larger ones (asymmetric cortex) up to 2 mm.  
226 Rosettes of sulphate minerals and bipyramidal quartz crystals are present within the oolites.

227 F3b includes aggregates (infra-mm to cm lumps and grapestones; Figs. 7D-F), intraclasts and oolites  
228 floating in a microsparitic matrix. Intraclasts are elongated fragments of mudstones or microbial  
229 laminites. Oolites are spherical to subspherical, asymmetric, micritic, and range from 500  $\mu\text{m}$  to 1.5  
230 mm in diameter.

231 F3c consists of homogeneous mudstones (Fig. 5D) or peloidal laminar wackestones to grainstones  
232 (Fig. 5F) with peloids, oolites or proto-oolites. Angular, planar, cross-stratifications and herringbone  
233 cross-beddings are common. The mudstone contains pyrite, pseudomorphs of sulphate minerals,  
234 organic matter fragments, detrital quartz, feldspars, and micas. Replaced acicular rods and nodules of  
235 sulphate (anhydrite relics) are present.

#### 236 Interpretation

237 F3a likely formed between 1 to 6 m in water depth and more likely around 2 m-deep (Keith  
238 and Zuppann, 1993) in high-energy shoals as attested by the occurrence of concentric oolites.

239 The shoals were later shortly exposed, as indicated by the presence of large asymmetric ooids  
240 or vadoids (Beukes, 1983). Evaporite reflux or hypersaline conditions are shown by the  
241 growth of sulphate crystals and bipyramidal quartz which are similar to those described by

242 Shukla and Friedman (1981) and by Mamet and Pr  at (2005). The sedimentary structures in  
243 F3a point to waves and tidal currents reworking as attested by cross-beddings, herringbones  
244 and asymmetrical ripples (Chakraborty, 2004; Boulvain, 2010).

245 F3b-c were deposited in low- to moderate-energy shallow waters located behind oolitic barrier  
246 complexes (Bathurst, 1971) in the subtidal, intertidal and supratidal lagoonal environments,  
247 locally disturbed by storms (Enos, 1983; Tucker et al., 1990). The sediments were submitted  
248 to hypersaline conditions as shown by the pseudomorphs of evaporitic minerals.

249

250 *5.4. Facies association 4 (FA4)*

251 FA4 consists of pisoid floatstones (F3d), intraformational conglomerates (F4), laminar detrital

252 mudstones (F5) and stratiform stromatolites (F6).

253

254 Description

255 F3d consists of pisoid floatstones with asymmetric ooids (1.5 to 2 mm in diameter), peloids

256 and remains of microbial mats (Figs. 9A,D). The pisoids (2 mm to 5 cm in diameter) are

257 irregular, elongate or oval (Figs. 9B-C). Desiccation cracks, keystone vugs, pseudomorphs

258 after anhydrite (even in the pisoid nucleus) are common. Meniscus and pendular cementation

259 are observed, pointing to the presence of typical beach-rock. Intensive fragmentation formed a

260 breccia (F4).

261 F4 is a stratified conglomerate including micritic and centimetric intraclasts with rare 'ghosts'

262 of ooids giving a characteristic "puzzle" texture. Spiny and half moonlike oolites are

263 common. Desiccation cracks, calcitized laths or nodules of anhydrite and authigenic

264 bipyramidal quartz crystals are regularly observed.

265 F5 is laminar clayey detrital mudstones (Fig. 10) with detrital content up to 30% (dominant quartz and

266 feldspars) with alternations of light-colored laminae (silty fine sand to fine silt) and dark-colored

267 laminae (dominant pyrite). Desiccation-cracks and organic matter fragments are also associated.

268 F6 consists of gently wavy, flat-laminations with domal structures (Figs. 5E-F). Laminae consist of

269 alternation of darker organic-rich (with pyrite framboids) and lighter organic-poor layers. The matrix

270 contains dispersed idiomorphic dolomite rhombs (up to 50  $\mu\text{m}$ ). The laminae are sometimes slightly

271 slumped and lenticular, deformed by crystallization of sulphate minerals occurring as microtepees.  
272 Fenestral and crinkled fabrics, and near horizontal sheet-cracks associated with vertical mud-crack are  
273 common.

274

#### 275 Interpretation

276 FA4, including F3d to F6, represents peritidal environments submitted to periodic emersions.  
277 F3d is indicative of vadose conditions on high-energy shoals with development of asymmetric  
278 ooids, pendular and meniscus cements during emersion. This environment is similar to the  
279 hypersaline supratidal zone in the Persian Gulf characterized by abundant pseudomorphs of  
280 anhydrite (Scholle and Kinsman, 1974). F4 represents a low-energy shallow-water upper  
281 intertidal to supratidal environments overprinted by episodic subaerial and marine-vadose  
282 diagenesis. Such sediments were sporadically subject to evaporation in hypersaline conditions  
283 as recorded by the precipitation of sulphates (Shearman, 1963; Kinsmann, 1969), spiny and  
284 half-moon ooids (Flügel, 2004). Laminae associated with mud-cracks in F5 point to a low-  
285 energy tidal flat environment in an upper intertidal to supratidal setting (Hardie, 1977;  
286 Sellwood, 1986; Clough and Goldhammer, 2000). F6 is interpreted as evaporitic-dominated  
287 low 'algal' marshes fringing ponds of channeled belts, similar with the Andros Island,  
288 particularly along the backslope of the levees and the beach-ridge washovers (Hardie and  
289 Ginsburg, 1977).

290

#### 291 *5.5. Facies association 5 (FA5)*

#### 292 Description

293 FA5 includes only clayey silty carbonates and dolomudstones (F7). It consists of stratified darkish  
294 microparitized dolomicrite matrix with remnants of microbial mats (Figs. 11A-C). Slumping and  
295 small-scale folding are observed. Sulphate (anhydrite, gypsum and polyhalite?) minerals are common  
296 and consist of lath-shaped and rosette-like aggregates (Figs. 11D-E), enterolithic nodules, veins,  
297 collapse breccias and castellated crystals (*sensu* Clark, 1980).

298

### 299 Interpretation

300 FA5 points to an evaporitic peritidal environment (intertidal, temporarily emerged in the  
301 supratidal zone), analogous to the recent littoral lagoons or sabkhas formed under warm semi-  
302 arid conditions, along the Persian Gulf and the Mediterranean Coast (Patterson and Kinsman,  
303 1981).

304

### 305 *5.6. Interpretation of depositional settings (Fig. 12)*

306 The SCI<sub>c</sub> Formation was deposited in a shallow ramp setting (*sensu* Burchette and Wright, 1992). It  
307 exhibits clayey mudstones, microbial silty mudstones (outer-ramp), stromatolite biohermal, HCS  
308 cross-bedded oolitic packstones/grainstones (mid-ramp) and vadose oolitic grainstones with  
309 homogeneous wackestones and laminar microbial bindstones, capped by evaporate dolomudstones  
310 (inner-ramp). The sediments were submitted to hypersaline conditions as shown by the abundant  
311 pseudomorphs of evaporitic minerals.

312 The outer-ramp was a site of accumulation of terrigenous clay, silt and carbonate mud with microbial  
313 MISS colonization in the quiet waters of the upper offshore at a depth of around 50 meters (FA1). The  
314 most common mid-ramp facies are typical of shoreface transition environments with storm-wave

315 deposition of HCS oolitic series and giant stromatolites development with inter-reefal stromatoclast  
316 accumulations (FA2). The inner-ramp facies are heterogeneous with high-energy environments in  
317 oolitic sandy shoals, forming a nearshore variably effective barrier with lenticular units and low  
318 energy environments in lagoonal settings behind the barrier. The inner-ramp facies are located above  
319 the fair-weather wave base from the high-energy shoal and the low energy back-shoal (FA3) to inter-  
320 and supratidal high energy beach proximal backshore environments with vadose cementation  
321 (meniscus and pendant cements) and planar microbial mats (FA4) passing laterally to the sabkha  
322 environments with hypersaline dolomudstones (FA5).

323

## 324 **6. Sequence Stratigraphy**

### 325 *6.1. Analysis of high-frequency cycles*

326 Sequence stratigraphy based on the recognition of sedimentary facies and unconformity surface  
327 relationships have provided a predictive framework for the evolutionary history of the SCI<sub>c</sub> Formation.  
328 The 27 sections (2 m to 57 m-thick) show the repetition of complete and incomplete cm to m-scale  
329 sequences. The cyclicity is pervasive throughout the SCI<sub>c</sub> Formation and generally easy to identify in  
330 the field. Five 'ideal' high-frequency shallowing-up cycles (5<sup>th</sup> order) are recognized in the SCI<sub>c</sub>  
331 Formation (Fig. 13 and Table 3); they are grouped in two main categories: (i) D-cycles (with D for  
332 'deep') bounded by marine flooding surfaces, across which facies deepen and (ii) S-cycles (with S for  
333 'shallow') bounded by subaerial exposures.

334 D cycles (2 m to 20 m-thick) are recognized from the lithological curve when a reset of F1 and/or F2  
335 occurs while S cycles do not contain F1 and/or F2. The D cycles are homogeneous, displaying mainly  
336 F1 and F2, their thicknesses are highly variable depending of the growth of the stromatolites up to 20

337 meters (F2). Evidence for major drowning unconformity in the SCI<sub>c</sub> succession is provided by the clay  
338 sedimentation associated with the MISS facies (see FA1, above) and by the development of giant  
339 stromatolites initiating D1 and D2 cycles. The upper part of D-cycles is related to F6 with or without  
340 typical products related to emersion or erosion.

341 S-cycles are centimetric-decimetric to 5-7 m-thick and show a shallowing-upward evolution, when  
342 complete, near subaerial exposure conditions are recorded at their tops. They show evolution from an  
343 oolite shoal to exposure surface associated with a sabkha environment: (i) the S1 cycle or ‘oolite shoal  
344 cycle’ starts with F3a-b, (ii) the S2 cycle or ‘lagoonal cycle’ starts with F3c and (iii) the S3 cycle or  
345 peritidal cycle starts with F3d. They contain several surfaces that can be erosive due to the scouring of  
346 oolite shoals by currents, frequent in shallow-water carbonates (Tucker and Wright, 1990; Strasser,  
347 2016). The S cycles are rather thinner and heterogeneous with a great variability in their facies  
348 composition recording a shallow-water sedimentation sometimes with non-deposition in the supratidal  
349 settings exhibiting numerous ‘hiatal’ surfaces. Their succession records high-frequency relative sea-  
350 level changes in the upper part of the shallow shelf.

351 The stacking pattern of the shallowing-upward D and S m-scale cycles led to the recognition of  
352 deepening and shallowing up parasequence sets (fourth-order, see below). Two typical sections (Saris  
353 and D sections) are presented here as they allow following the successions of a few cycles (Figs. 14-  
354 15; Table 4; Ackouala Mfere, 2017).

355 The parasequence sets (fourth-order) of both sections (and all others in Ackouala Mfere, 2017) are  
356 aggradational and progradational.

357 The parasequence set package, deduced from the D and Saris section, is also recognized in many other  
358 sections in the Niari-Comba subbasins of the NWCB from Zanzo at the East to Soulou at the West,

359 over more than 80 km (Fig. 3). As in Lout  t   (Sonocc quarry, Pr  at et al., 2018), it also consists of the  
360 succession of the S1, S2 and S3 elementary cycles forming shallowing-upward packages.

361

## 362 *6.2. Sedimentary belts, Flooding (F) vs Forced Regression (FR) surfaces*

363 On the basis of the facies associations, we recognize at least three major successions which are partly,  
364 or not entirely, superimposed as their precise succession cannot be specified due to the small thickness  
365 of each of the studied sections (< 60 m, average  $\pm$  15-20 m). Each succession is characteristic of a part  
366 of the ramp system and shows the succession of facies as follows (Fig. 16): ORS (outer-ramp  
367 succession) with FA1, MRS (mid-ramp succession) with FA2, IRS (inner-ramp succession) with FA3-  
368 4-5. Each succession is formed by the stacking of meter-scale shallowing-upward 5<sup>th</sup>-order or high-  
369 frequency cycles (Ackouala Mfere, 2017). ORS succession (from W to E; example with sections O, F,  
370 D) is generally thin-bedded and grades up into the massive stromatolitic bioherms of the MRS  
371 succession (from W to E; sections T, N, P, F, K, H, B and MAD8019). MRS succession, comprising  
372 the massive stromatolitic bioherms (e.g., from W to E; sections T, Q) shows oolitic units with HCS.  
373 IRS succession consists of thin- to thick-bedded oolitic units (0.5 to 5 m thick) with trough, planar and  
374 herringbone cross-laminations and homogeneous lagoonal units (from W to E, mainly in sections  
375 MAD8016, O, M, F, H, D, B, MAS8018, MAD8019). Low-angle clinofolds are present suggesting  
376 prograding washover oolitic deposits on the stromatolite bioherms (sections P and Q). The  
377 interdigitation (not frequent) and the sharp (common) contacts observed in these two profiles between  
378 the oolites and the massive bioherms indicate that the oolitic sands migrated partly during, and mainly  
379 after, the biohermal growth.

380 Based on the different sections, IRS succession is the thickest (up to 55 m) and the ORS the thinnest.  
381 The latter is probably thicker because, as being made of clays, it is easily weathered and thus good  
382 outcrops are rare. The oolitic shoal has varying thicknesses of a few meters up to about a minimum of  
383 30 m (section Q).

384 Lateral relationships between the three successions and their 4<sup>th</sup> and 5<sup>th</sup> order packages can be deduced  
385 from sections T, N, P, Q?, F, K, H, D, B, MAD8019 as all these sections exhibit a marine flooding  
386 surface, despite the packages they form, are not time constrained:

387 (i) most of the above mentioned profiles (F, K, H, D, B, MAD8019) have a similar stacking pattern  
388 with alternation of meter-scale FA3/FA4. Lateral thickness variations cannot be established as the  
389 sections are limited to the outcrop exposure, but it seems that for the thicker sections, the general  
390 FA3/FA4 successions exhibit a similar thickness (~20-25 m) except in MAD8016 /MAD8018 with the  
391 thickest thicknesses (at least twice or more if compared with the other sections). These alternations are  
392 mostly composed of 5<sup>th</sup> order shallowing-upward S2 and S3-cycles with vadose diagenesis in the  
393 pisoid grainstones (see sub-chapter 5.1), these cycles are grouped in 4<sup>th</sup> order parasequence sets  
394 (Ackouala Mfere, 2017);

395 (ii) thick stacks (at least 30 m, section Q) of amalgamated packstone/grainstone shoal complexes  
396 (FA3 *pro parte*) separating distally downdip biohermal stromatolites (FA2 *pro parte*). The dominantly  
397 5<sup>th</sup> order progradational cycles (S1 cycles) are rather badly preserved due to the wedge-shaped cross-  
398 beddings with planar and trough bedforms up to 1 m-thick and numerous inclined discontinuities  
399 representing reactivation surfaces during storm-dominated processes (including HCS);

400 (iii) thin stacks (2-10 m-thick, sections T, F, D, B, MAD8018) of deeper facies assemblages (FA1 and  
401 FA2 *pro parte*) with a few D aggradational cycles (subchapter 6.1).

402 In the different field sections, we recognized two types of erosional surfaces: marine flooding and  
403 forced regression surfaces. Marine flooding surfaces ('F' surfaces) are characterized by a sharp  
404 deepening upward in the depositional environments from inner to outer ramp deposits (from W to E;  
405 sections T, N, P, Q?, F, D, B, MAD8019, in this latter section three repeated flooding surfaces are  
406 present; Fig. 16). One of them, being the only continuous surface, correlates laterally over long  
407 distances, is interpreted as a transgressive surface (TS surface). Forced regression surface (FR surface)  
408 is also recognized in most places. It is marked by an abrupt passage from offshore facies of the outer  
409 ramp (FA1) to the shallow-water inner-ramp facies (FA4) (from W to E; sections O and F) with no  
410 evidence of extensive subaerial exposure. In most places, the FR surface underlines prograding oolitic  
411 shoal deposits. This surface originates from a falling stage of the base level from the offshore to the  
412 proximal backshore, which in our succession represents a sea-level fall of a few tens of meters as  
413 facies FA1 ( $\pm$  40-50m deep) is directly covered by facies FA4 (0-10 m deep).

414 From the detailed analysis of the 27 sections, we propose an 'ideal' or 'virtual' synthetic SCI  
415 succession. It starts with section MAD8019 (with three flooding surfaces), overlain by section Q with  
416 the thickest oolite shoal above a FR surface (Fig. 16) and covered by section MAD8018 (with the  
417 thickest peritidal facies and silty evaporites at the SCII boundary). The oolite shoals and reefal bodies  
418 are parallel and accumulated along a W-E 100 km-long regional axis bordering the Archean Congo  
419 Craton located in the North. Based on the recently revised geological map and personal information of  
420 BRGM (pers. communication, Y. Callec, BRGM) the width of the oolite shoal is about 30-60 km.

421

## 422 **7. Discussion**

423 *7.1. Distribution of stromatolites in the Niari-Nyanga and Comba subbasins of the NWCB*

424 Giant stromatolitic bioherms are more developed in the eastern part of the studied area while  
425 they are rare and thin (less than 1 m) in the western part (Fig. 16) reflecting probably the  
426 variation of the accommodation space.

427 Growth of the main reef builders is affected by a multitude of environmental factors, such as  
428 temperature, illumination, turbidity, substrate, and nutrients levels. Many of these factors vary  
429 systematically with depth, and this has led to recognition of reefal depth-related zonations in  
430 the Phanerozoic rocks (James and Bourque, 1992), and in the early Neoproterozoic series  
431 (Bertrand-Sarfati and Moussine-Pouchkine, 1985; Sarkar and Bose, 1992). Alvarez and  
432 Maurin (1991) described a NE deepening of the basin with the development of giant  
433 stromatolitic bioherms located at the “junction” between the Niari-Nyanga and Comba  
434 subbasins of the NWCB (Bertrand-Sarfati and Vicat, 1987; Trompette and Boudzoumou,  
435 1988). Variation of the accommodation space has controlled the shape and the vertical  
436 development of the reefs in the SCI<sub>c</sub> Formation. Giant stromatolitic bioherms grew during a  
437 relative high sea-level where light and oxygen were sufficient to promote the activity of  
438 cyanobacteria as shown previously with the stacks of bodies up to 20 m in height. On the  
439 contrary, the flat and laminar stromatolites with small domes (< 80 cm) recorded a  
440 progradational phase, most likely because limited accommodation space did not permit  
441 development of giant stromatolites.

442

#### 443 *7.2. Evidence of storm events in the carbonates of the SCI<sub>c</sub> Formation*

444 The oolitic grainstones-packstones show undulating bedding referred to as HCS (Dott and Bourgeois,  
445 1982; Duke, 1985; Morsilli and Pomar, 2012), indicative of storm events in the shoreface transition as

446 the greatest potential preservation of these structures is between the fair weather- and storm-wave  
447 bases, that is a few to several tens of meters (Dott and Bourgeois, 1982; Dumas and Arnott, 2006).  
448 These high-energy conditions bring a large amount of sediment into suspension near the sea floor and  
449 the mixture of sediment and water oscillates back and forth from shallow to deep waters. Although  
450 most oolites form in wave-dominated shallow water shoals (commonly about 2 m), these grains are  
451 readily dispersed by storm return currents in deeper water settings.

452 The general successions exposed in the oolite shoals usually reveal an upward transition from HCS to  
453 low-angle tabular cross-bedding. This transition reflects an increase in water hydrodynamics and a  
454 shallowing up trend from shoreface to beachface environments. Prograding sequences have been  
455 documented in many successions with storm effects indicating an upward decrease in water depth  
456 (Dott et Bourgeois, 1982), as in an Indian Neoproterozoic ramp (Chakraborty, 2004) and in the  
457 Neoproterozoic Bambuí basin of central-eastern Brazil, which lays on top of the same craton with the  
458 West Congo units on the other side of the Atlantic (Uhlein et al., 2019).

459 In the SCI<sub>c</sub> Formation, high-energy events are also attested by the elongated stromaclasts (up  
460 to 5 cm in length) accumulated in inter-reef areas between the stromatolites. These high-  
461 energy events were probably related to episodic storms that formed the HCS in the oolite  
462 shoals.

463

### 464 *7.3. Development of systems tracts*

465 In the absence of time constraints on sequence stratigraphy hierarchy, the key physical  
466 bounding surfaces (flooding and forced regression) and the stacking pattern analysis of high  
467 frequency cycles (S vs. D) help in deciphering the stratigraphic pattern in the basin. The SCI

468 is interpreted as a single third-order transgressive-regressive sequence which includes a  
469 transgressive systems tract (TST) and a highstand systems tract (HST) after the post-Marinoan  
470 deglaciation event (Alvarez, 1995). We here interpret the SCI Subgroup as two transgressive-  
471 regressive third-order sequences (Fig. 17). In the first sequence, TST sedimentation started  
472 with deposition of the 10-12 m-thick cap carbonates (SCI<sub>a</sub>) and about 10-15 m-thick of  
473 siliciclastic deposits (lower SCI<sub>b</sub>). This latter is followed by an HST phase (upper SCI<sub>b</sub>, about  
474 135 m-thick) above a maximum flooding surface (MFS). In the second sequence starting with  
475 the SCI<sub>c</sub>, a lowstand systems tract (LST) is initiated with very shallow water deposits  
476 characterized by the alternation of FA3/FA4 with abundant S2 cycles. The LST is overlain by  
477 a TS leading to the development of the 'deep' MISS facies (TST). The MFS above the TST is  
478 followed by a HST (giant stromatolites). Favorable environmental conditions helped by high  
479 accommodation rates after deposition of mud and siliciclastic layers (MISS facies in our case)  
480 resulted in growth of giant stromatolites as described in the Proterozoic ramp of Australia  
481 (Sami et al., 2000). Stromatolite growth was surely unable to keep pace with initial sea-level  
482 rise, resulting in the deposition of mud-dominated sediments (MISS facies), which probably  
483 represents a "condensed" interval.

484 The HST is marked by complete or incomplete aggradational shallowing-upward cycles as  
485 shown in Zanzo, B, D, H, K and F sections (Fig. 16). Laterally, the giant stromatolites  
486 interfinger with hummocky cross-bedded oolitic grainstones.

487 In most places, the giant stromatolites are sharply buried by trough cross-bedded oolitic  
488 grainstones (S1 cycles) in a forced regression systems tract (FRST) evolving to subtidal and  
489 peritidal facies near emersion (S2 and S3 cycles), when reduced accommodation rates

490 facilitated the accumulation of the shallowest facies. In some sections, interdigitation with  
491 lateral pinch-outs between the giant columnar stromatolites (F2) and the oolite shoals (F3) has  
492 been observed. They can be followed laterally over a minimum of a few meters, depending on  
493 the size of the outcrops. This interdigitation represents a lateral facies change from giant  
494 columnar stromatolites to oolite shoals, which also overlay the stromatolites. Thick oolite  
495 shoal stacking units, above the FR surface (see sections T, Q) shows that progradation  
496 accelerated with time during the FRST probably due to a net fall of sea-level. Sea-level fall  
497 could also be recorded in section Q with exposed areas of carbonate sediments, which  
498 produced oolite dunes or large-sized lenses (sections Q and R) as a result of tidal processes.  
499 At the transition to SCII, the succession is marked by deposition of silty evaporites and  
500 dolomites at the top of MAD8018 section (Fig. 16). These silty evaporites and dolomites  
501 represent a LST of the next sequence in the SCII series. (Fig. 17).

502

503 *7.4. Facies correlations between the Niari-Nyanga and Comba subbasins in RC to the Lower Congo*  
504 *subbasins in DRC*

505 The C3 Formation (SCI<sub>c</sub> equivalent in Lower Congo, DRC) about 240 m-thick, dominantly contains  
506 light-grey limestones with greenish-grey shales (C3a Member), and massive to crossed-bedded light  
507 grey to whitish oolitic and pisoid limestones with thin layers of greenish shales and intraformational  
508 conglomerates (C3b Member) (Lepersonne, 1974; Cailteux et al., 2015; Delpomdor et al., 2015,  
509 2019). The standard sequence starts with open marine environments and oolitic shoals passing to  
510 restricted peritidal/sabhka environments behind the oolite shoals in a mid- to inner-ramp setting  
511 (Delpomdor et al., 2015, 2019). Due to the long distance (around 150 km between the sections in RC

512 and DRC) and the absence of globally-correlative marker levels in these unfossiliferous series, the  
513 current correlation of SCI<sub>b</sub> and SCI<sub>c</sub> with respectively C2 and C3 series is a quite simplistic useful  
514 interpretation; see Fig. 17. For example, the lowermost part of the SCI<sub>b</sub> series consisting of marls and  
515 marly limestones, locally limestones in the loop of the Niari river (Dadet, 1969), could be coeval with  
516 the lowermost part of the C2 Formation (e.g., C2a to C2c members; stratigraphic correlation after  
517 Cahen, 1978), while the uppermost part of the C2 Formation (e.g., C2d to C2e members) consisting of  
518 calcareous shales, sandy and muddy limestones and limestones (Delhayé and Sluys, 1923;  
519 Lepersonne, 1974; Cailteux et al., 2015; Delpomdor et al., 2015) could be coeval with the upper part  
520 of the SCI<sub>b</sub> Formation, which is mainly constituted of marly limestones and limestones (Dadet, 1969).  
521 The lowermost member of the SCI<sub>c</sub> series (e.g., SCI<sub>c-a</sub> Member) could be laterally coeval with the C2f  
522 to C2g members of the C2 Formation, which consist of calcareous shales, sandstones and limestones.  
523 The C3 Formation, divided into C3a and C3b members (Cailteux et al., 2015) is proposed in this study  
524 as coeval with the lower and upper part of the SCI<sub>c</sub> series respectively. Correlation from these  
525 shallow-water series with multiple shoaling events deduced from the lithologic patterns is therefore  
526 difficult and could be improved by using the sequence stratigraphy data of our work in RC and the  
527 study of Delpomdor et al. (2015) in DRC. These marine deposits formed in extensive near shore  
528 environments during a global transgression related to the probable deglaciation at the end of Snowball  
529 Earth. In both areas, the shelf was block-faulted and structured into highs and shallow depressions,  
530 creating complex morphologies as suggested by Alvarez and Maurin (1991) in the Niari-Comba area.  
531 Our detailed stratigraphic sequence analysis of the Comba aulacogen combined with paleobathymetric  
532 data allows correlation of third-order sequence between the two areas (RC and RDC) (Fig. 17). This  
533 reveals that the SCI<sub>b</sub> is partly related to a TST phase (SCI<sub>a</sub> and lower SCI<sub>b</sub> in RC or C2a-b members in

534 DRC) and an HST phase (upper SCI<sub>b</sub> in RC or C2c-e members in DRC). The extreme uppermost part  
535 of the C2 formation, e.g., C2f to Ce2h members; observation by Sikorski, 1958) in DRC could  
536 laterally correspond to facies recording a LST in RC, and the C3a Member to TST and HST recorded  
537 in the lowermost part of the SCI<sub>c</sub> series in RC, if we consider that the giant stromatolites never  
538 described in DRC are included in this formation. After the lowstand to highstand sequence, the oolite  
539 shoals (C3b Member) or the uppermost part of the SCI<sub>c</sub> is newly reinterpreted as FRST marked by the  
540 progradation of oolite shoals evolving to peritidal facies near emersion atop of the SCI<sub>c</sub> series and C3  
541 Formation, when reduced accommodation rates facilitated the accumulation of shallowest facies. As  
542 suggested by Delpomdor et al. (2015), the top of the C3 Formation has been exposed to erosion/and or  
543 karstification suggesting a regional-scale turn off the carbonate factory. In this context, the silty  
544 evaporates at the transition SCI-SCII are interpreted as a LST in the next sequence (SCII Formation in  
545 RC or C4 in DRC).

546 However, we interpret the three positive jumps of the Fischer plot present in the C3a2 to C3b2 units  
547 (Delpomdor et al., 2015) as probably related to reactivations of the block-faulting observed in the SCI<sub>c</sub>  
548 Formation, in this case related by flooding surfaces (Fig. 16). Both areas experienced basin tectonics  
549 in the general context of a pre-collisional phase creating changes in relative sea-level by reactivation  
550 of pre-existing faults. This implies that the parasequence packages are strongly controlled by tectonics  
551 and are diachronous on the scale of the whole basin. Our sequence stratigraphic analysis allows for the  
552 first time tentative correlation in the Schisto-Calcaire Group and Lukala Subgroup in RC and DRC  
553 respectively. Giant stromatolites observed in RC were identified in the lowermost part of the SCI<sub>c</sub>  
554 series, while stromatolitic reefs (10 m long and a few meters width), associated with breccias and  
555 oolitic limestones have been found in the C3b Member (Cahen, 1950). Recently, microbial mats have

556 been identified in the C3a Member in DRC (Delpomdor et al., 2015). As shown previously, water  
557 depth is the first-order control on reef growth and morphology. Deep water is essential for  
558 development of giant stromatolites but cyanobacteria need also fine grained sand substrate for best  
559 development, as shown previously with the MISS of the F1 (Noffke, 2010). Giant domal stromatolites  
560 commonly form in deep water settings (Bertrand-Sarfati and Moussine-Pouchkine, 1985; Dill et al.,  
561 1986; Glumac and Walker, 2000) while flat morphologies occur in shallow water settings (Arenas and  
562 Pomar, 2010; Glumac and Walker, 2000). Water depth was probably higher in the sedimentary areas  
563 located in RC than in the DRC as a result of the structuration of this area by tectonic effects during  
564 sedimentation. Although the geometry of deposits of the SCI<sub>c</sub> Formation is seen as continuous on the  
565 southern edge of the Chaillu Massif, Chorowitz et al. (1990) concluded that the Lower Congo/Sangha  
566 aulacogen, extended to the Comba aulacogen, shows multiple pull-apart-type tectonic areas  
567 constituted of elongated WNW-ESE tilted blocks defined by NE-SW faults. Therefore, the  
568 sedimentation records the development of oolite shoals. The development of a cordon of oolitic sands  
569 of the C3 Formation in DRC, similar to the SCI<sub>c</sub> Formation of RC, may also be inferred on the NW  
570 edge of the Kasai block. The oolitic shoals seem to bypass the NW Kasai block by the thickening of  
571 oolitic limestones (100-200 m in thickness) in Angola (Schermerhorn and Stanton, 1963).

572

### 573 *7.5. Origin of cyclicity*

574 Facies analysis led to the recognition of a cyclic pattern in the SCI<sub>c</sub> sedimentation. Generally, the  
575 recognized cycles exhibit a shallowing-upward trend, as suggested by the vertical facies evolution  
576 along the standard sequence. Autocyclic and allocyclic mechanisms can both lead to shallowing-  
577 upward cycles (Strasser, 1991). While autocyclic processes operate within the sedimentary basin with

578 progradation of tidal flat or lateral migration of tidal channels (Satterley, 1996), allocyclic control  
579 mechanisms are independent of the depositional processes and include eustatic sea-level fluctuations  
580 (Elrick, 1995) or repeated synsedimentary tectonic downfaulting events, e.g., tectonics model  
581 proposed by Cisne (1986). Subsidence does not appear to have been constant during deposition of  
582 SCI<sub>c</sub> Formation over the whole studied area as the SCI<sub>c</sub> thicknesses show important variations; rather  
583 it was affected by periodic changes. On the other hand, SCI<sub>c</sub> cyclic deposition (fourth-order) is not  
584 harmonious, and the cycles are difficult to correlate between neighboring sections (less than a few  
585 kilometers) despite the overall regressive depositional trend of the stratigraphic interval and the  
586 consistent shallowing-upward parasequence trend within the sections.

587 There are a variable number of elementary parasequences (fifth-order) at each locality suggesting that  
588 most are probably the result of migration of local environments due to multiple shoaling events. In this  
589 context, these parasequences seem to be autocyclic (Ginsburg, 1971) and represent the typical  
590 evolution (migration, erosion, non deposition) of ooid dunes controlled by currents and sea-level  
591 fluctuations at very shallow depths. Moreover, accumulation rate variations and diagenesis could also  
592 modified the final shapes of the SCI<sub>c</sub> stratigraphical data sets. Additionally, several subaerial  
593 exposures of the investigated sections and erosional boundaries suggest periodical drops of the relative  
594 sea-level followed by renewed transgressions.

595 Assuming that the autocyclic mechanism originated from aggradational/progradational trends during  
596 deposition of the SCI<sub>c</sub> Formation, this process suggests a particular factor affecting the Niari-Nyanga  
597 and Comba subbasins of the NWCB to drive the changes in the accommodation space. A tectonic  
598 control with reactivation of pre-existing faults (leading to multiple episodes of accommodation space  
599 changes) may play a role in the origin of these cycles (see below, 6.6.)

600 The fact that D1 cycles are directly overlain by progradational facies suggests that there was no true  
601 drowning and they were not associated with a true eustatic sea-level increase. They have been related  
602 to local interference by tectonic movement or autocyclic processes. The lateral and vertical  
603 variabilities of thickness of the elementary parasequences could be attributed not only to the variable  
604 potential of sediment accumulation in the different environments (shoal, back-shoal, tidal channels,  
605 lagoon, shoreface) but also to the tectonic context that created the Niari-Comba subbasins of the  
606 NWCB. As a result, random processes dominated and blurred the low-amplitude sea-level signal, and  
607 the resulting sedimentary records will differ depending on their location in the basin (Strasser, 2016).  
608 The sedimentary environments were generally shallow enough to record the several relative sea-level  
609 fluctuations (1-5 m) and produced the common observed S-cycles. As no order or regularity in the  
610 cycle pattern is observed, as could be expected if orbital forcing was the dominant mechanism, it is  
611 highly probable that autocyclic processes (helped or inferred by tectonics) were dominant, in a general  
612 tectonic setting with both constant and differential subsidence along various faulted blocks.

613

#### 614 *7.6. Tectonic significance and regional implication*

615 All of the high-order cycles identified in the SCI<sub>c</sub> Formation were deposited under conditions of sea-  
616 level fluctuations driven by tectono-eustasy, which dominated the late Neoproterozoic.

617 During Neoproterozoic times, several distinct extensional tectonic episodes affected the São  
618 Francisco-Congo Craton in the area related to the development of the AWCO (Pedrosa-Soares and  
619 Alkmin, 2011). After 660 Ma, a passive margin developed in the WCB with deposition of the  
620 Bouenza-Louila Subgroup in RC, the stratigraphic equivalent Haut-Shiloango Subgroup in DRC,  
621 followed by respectively the Upper Diamictite Formation and the Lukala Subgroup (Frimmel et al.,

622 2006; Poidevin, 2007). These movements in the basin reflected pre-Marinoan extensional events (see  
623 Pedrosa-Soares and Alkmin, 2011), enhancing tectono-eustatic fluctuations during the pre-, syn- and  
624 post-sedimentary deposition (Delpomdor et al., 2015, 2016, 2019). Under these passive margin  
625 conditions, the relative eustatic variations in the SCI<sub>c</sub> Formation are the consequence of short-time  
626 extensional tectonic activities in the whole basin including several sub-events in Central Africa and  
627 recorded through the fifth-order D- and S-cycles. Deepening occurred when relative sea-level and/or  
628 accommodation space increased due to short-time extensional tectonic activities leading to the  
629 drowning of the former inner-ramp areas.

630 The same cyclicities have been recognized in the C3 Formation in Lower Congo (Delpomdor et al.,  
631 2015, 2019). The tectonics was probably related to the breakup of Rodinia which influenced  
632 sedimentary processes through tectonic subsidence and sediment supply in a similar way as occurred  
633 along opposing paleo-Atlantic and paleo-Pacific margins of Laurentia (Eyles and Januszczak, 2004).

634 Even if the timing of the series is poorly constrained in order to establish detailed correlations between  
635 the lower part of the Schisto-Calcaire Group in SW Gabon (Préat et al., 2010), Lower Congo region  
636 (Delpomdor and Préat, 2013) and our studied area, it appears that the SCI<sub>c</sub> overlying the reddish  
637 calcareous marls and marls (SCI<sub>b</sub> Formation) is coeval with the Nsc1c (Préat et al., 2011, 2018), and  
638 probably the top of the C2 Formation and with the C3 Formation in Lower Congo region (DRC;  
639 Delpomdor et al., 2015). As shown by Delpomdor et al. (2015, 2019) and in our study, this  
640 sedimentation exposes mainly shallowing-upward cycles in response to tectono-eustasy occurring in  
641 the late Neoproterozoic (Tack et al., 2001; Li et al., 2008; Delpomdor and Préat, 2013). In RC, general  
642 sea-level rise did not occur in one continuous phase as highlighted by the recurrence of the D1 cycles  
643 in (D, H, Zanzo, F and T sections; Fig. 16), but was probably triggered by the reactivation of regional

644 block-faulting (see Strasser, 2016 for general consideration) with extensional faults related to the  
645 rifting evolution of the Comba aulacogen (see above). The lateral variability in the thickness of the  
646 elementary parasequences (Ackouala Mfere, 2017) is therefore attributed not only to the variable  
647 potential of sediment accumulation in the different environments but also to syndimentary tectonics.

648

## 649 **8. Conclusions**

650 The SCI<sub>c</sub> Formation was formed in a paleoramp setting from quiet water in the outer-ramp (FA1) to  
651 very shallow water under hypersaline conditions in the inner-ramp (FA5). Storm events have been  
652 recognized by HCS in the oolitic series and by elongate stromaclasts (up to 5 cm in length)  
653 accumulated in inter-reef areas between the stromatolitic bioherms (FA2). The SCI<sub>c</sub> Formation records  
654 LST, TST, HST and FRST successions (Fig. 17) linked to the reactivation of regional block-faulting  
655 and is also marked by a regional TS (Fig. 16). The D and S-cycles or elementary parasequences  
656 (meter-scale from 0.1 to 20 meters in thickness) are well developed in the carbonate ramp from outer-  
657 to inner-settings with dominant S1 cycles in high energy settings and lagoonal S2 cycles in low energy  
658 settings. The magnitude of the sea-level change was mostly small (except during the transgression and  
659 the forced regression), less than a few meters as deduced from the average of the tidal cycle thicknesses  
660 (1-3 m-thick). This produced a random stack of elementary parasequences, as for example where  
661 shoals migrated out of main transport path. The LST in the SCI<sub>c</sub> Formation is represented by the  
662 maximum of progradation of the whole SCI Subgroup, with decreasing circulation and fluctuating  
663 salinities, reflected by development of a sabkha environment with dolomudstones and abundant  
664 sulphate pseudomorphs (FA5), also pointing to a probable climate change from semi-arid to arid  
665 setting. The SCI<sub>c</sub> Formation records high-frequency shallowing-upward cycles generated by an

666 autocyclic mechanism that is likely controlled by tectonic syn-sedimentary extensional faults related  
667 to the rifting of the basin. On a broader scale, the recurrent generation of accommodation space was  
668 triggered by short-time extensional tectonic activity related to several sub-events in Central Africa.  
669 The cyclic succession of the fourth-order parasequences in the SCI<sub>c</sub> Formation has been correlated  
670 between the studied sections following the general trend. In detail, each section shows a specific  
671 evolution, as for example the FR observed in two sections. The stratigraphic package of the SCI<sub>c</sub>  
672 Formation can be subdivided into two broad 4<sup>th</sup>-order sequential units: the first one comprises  
673 packages of the laminar clayey silty mudstones (MISS facies) and stromatolite bioherms, the second  
674 starts with ooid shoals and is terminated by evaporative dolomudstones. This 'binome' formed of  
675 packages of elementary parasequences can be traced across the whole shelf, even while it is  
676 impossible to trace the individual parasequences and occurs over more than 100 km reflecting the  
677 sedimentary filling of the basin, which is probably tectonically driven. The elementary parasequences  
678 and their grouping are diachronic, they do not produce a clear stacking pattern, and cannot be used for  
679 chronostratigraphy. Their distribution is related to the amount of accommodation space available,  
680 which is primarily controlled by differential subsidence among the faulted-blocks. The best correlation  
681 across the basin (from Gabon to Angola) is surely the recognition of this 'binome'.

682

### 683 **Acknowledgements**

684 We want specially to thank Total Congo for sponsoring of this study carried out in the frame of a  
685 mapping project in the Republic of the Congo. We thank also Georges Zaboukis and Francisco  
686 Serbeto Ibanez for the thin section production. We acknowledge Scott Elrick (ISGS) for the helpful  
687 discussions and improving the English of the manuscript. We thank the reviewer Fabricío Caxito

688 and the editor Damien Delvaux for their constructive reviews and helpful criticism.

689

690 **Bibliography**

691 Ackouala Mfere, A.P., 2017. Sédimentologie, Cyclicité et Diagenèse des Carbonates de la Formation  
692 du Schisto-Calcaire (SCIC) dans les sous-bassins de Niari-Nyanga et de Comba en République  
693 du Congo, PhD thesis, Université Libre de Bruxelles, 265pp.

694 Affaton, P., Kalsbeek, F., Boudzoumou, F., Trompette, R., Thrane, K., Frei, R., 2016. The Pan-  
695 African West Congo belt in the Republic of Congo (Congo Brazzaville): Stratigraphy of the  
696 Mayombe and West Congo Supergroups studied by detrital zircon geochronology. *Precambrian*  
697 *Res.* 272, 185–202. <https://doi.org/10.1016/J.PRECAMRES.2015.10.020>

698

699 Allen, P.A., Leather, J., Brasier, M.D., 2004. The Neoproterozoic Fiq glaciation and its aftermath,  
700 Huqf supergroup of Oman. *Basin Res.* 16, 507–534. [https://doi.org/10.1111/j.1365-](https://doi.org/10.1111/j.1365-2117.2004.00249.x)  
701 [2117.2004.00249.x](https://doi.org/10.1111/j.1365-2117.2004.00249.x)

702

703 Alvarez, P., Maurin, J.-C., 1991. Evolution sédimentaire et tectonique du bassin protérozoïque  
704 supérieur de Comba (Congo) : Stratigraphie séquentielle du Supergroupe Ouest-Congolien et  
705 modèle d'amortissement sur décrochements dans le contexte de la tectogénèse panafricaine.  
706 *Precambrian Res.* 50, 137–171. [https://doi.org/10.1016/0301-9268\(91\)90051-B](https://doi.org/10.1016/0301-9268(91)90051-B)

707

708 Alvarez, P., 1995. Evidence for a Neoproterozoic carbonate ramp on the northern edge of the Central  
709 African craton: relations with Late Proterozoic intracratonic troughs. *Geol. Rundsch.* 84, 636-648.

710

711 Arenas, C., Pomar, L., 2010. Microbial deposits in upper Miocene carbonates, Mallorca, Spain.

712 *Palaeogeogr. Palaeoclimatol. Palaeoecol.* 297, 465–485.

713 <https://doi.org/10.1016/J.PALAEO.2010.08.030>

714 Arnaud, E., Eyles, C.H., 2006. Neoproterozoic environmental change recorded in the Port Askaig

715 Formation, Scotland: Climatic vs tectonic controls. *Sediment. Geol.* 183, 99–124.

716 <https://doi.org/10.1016/J.SEDGEO.2005.09.014>

717 Bathurst, R.G.C., 1971. *Carbonate sediments and their diagenesis*, Elsevier, Amsterdam.

718 [https://doi.org/10.1016/0016-7185\(73\)90072-9](https://doi.org/10.1016/0016-7185(73)90072-9)

719 Baudet, D., Fernandez, M., Kant-Kabalu, F. & Laghmouch, M., 2013. Carte géologique de la

- 720 République Démocratique du Congo au 1/500 000- Province du Bas-Congo. Musée royal de  
721 l'Afrique centrale, Tervuren, Belgique & Centre de Recherches Géologiques et Minières,  
722 Kinshasa, RD Congo, avec une notice explicative de 50p.
- 723 Bertrand-Sarfati, J., Moussine-Pouchkine, A., 1985. Evolution and environmental conditions of  
724 Conophyton-Jacutophyton associations in the Atar dolomite (Upper Proterozoic, Mauritania).  
725 Precambrian Res. 29, 207–234. [https://doi.org/10.1016/0301-9268\(85\)90069-5](https://doi.org/10.1016/0301-9268(85)90069-5)
- 726 Bertrand-Sarfati, J., Vicat, J.P., 1987. Les stromatolites columnaires du Schisto-Calcaire du  
727 Protérozoïque Supérieur du Congo et leur place dans la sédimentation. Bull. Société Géologique  
728 Fr. III, 289–298. <https://doi.org/10.2113/gssgfbull.iii.2.289>
- 729 Beukes, N.J., 1983. Ooids and oolites of the proterophytic Boomplaas Formation, Transvaal  
730 Supergroup, Griqualand West, South Africa, Coated grains. Springer Berlin Heidelberg, Berlin,  
731 Heidelberg. [https://doi.org/10.1007/978-3-642-68869-0\\_18](https://doi.org/10.1007/978-3-642-68869-0_18)
- 732 Bose, P.K., Chaudhuri, A.K., 1990. Tide versus storm in epeiric coastal deposition: Two Proterozoic  
733 sequences, India. Geol. J. 25, 81–101. <https://doi.org/10.1002/gj.3350250203>
- 734 Boulvain, F., 2010. Pétrologie sédimentaire des roches aux processus. Ellipses.
- 735 Burchette, T.P., Wright, V.P., 1992. Carbonate ramp depositional systems. Sediment. Geol. 79, 3–57.
- 736 Cahen, L., 1950. Le Calcaire de Sekelolo, le Complexe tillitique et la Dolomie rose C1 dans  
737 l'Anticlinal de Congo dia Kati (Bas-Congo). Annales du Musée royal du Congo belge, Tervuren,  
738 in 8°. Sciences Géologique. 7, 55 pp.
- 739 Cahen, L., 1978. La stratigraphie et la tectonique du Super- Nd isotope ratios are listed in Table 5.  
740 Ages were groupe Ouest-Congolien dans les zones me ´diane et externe calculated following  
741 Ludwig (1999). de l'orogène Ouest-Congolien (Pan-Africain) au Bas-Zaïre et dans les régions  
742 voisines. Ann. Mus. R. Afr. Centr., 3 Tervuren (Belg.), in-8°, Sci. Géol. 83, p.150
- 743 Carto, S.L., Eyles, N., 2012. Sedimentology of the Neoproterozoic (c. 580 Ma) Squantum “Tillite”,  
744 Boston Basin, USA: Mass flow deposition in a deep-water arc basin lacking direct glacial  
745 influence. Sediment. Geol. 269–270, 1–14. <https://doi.org/10.1016/J.SEDGEO.2012.03.011>
- 746 Chakraborty, P.P., 2004. Facies architecture and sequence development in a Neoproterozoic carbonate  
747 ramp: Lakheri Limestone Member, Vindhyan Supergroup, Central India. Precambrian Res. 132,

- 748 29–53. <https://doi.org/10.1016/J.PRECAMRES.2004.02.004>
- 749 Charles, N., Callec, Y., Pr at, A., Thi blemont, D., Delpomdor, F., Malounguila, D., Gloanguen, E.,  
750 Petitot, J., Ackouala, A.-P., Ndiele, B., Mvoula boungou, I., Moebo Boungou, M., 2015. Notice  
751 explicative de la carte g ologique de la R publique du Congo   1/200 000, Feuille Madingou.  
752 Editions BRGM, 225 pp.
- 753 Cailteux, J.L.H., Delpomdor, F.R.A., Ngoie Ndobani, J.-P., 2015. The Neoproterozoic West-Congo  
754 “Schisto-Calcaire” sedimentary succession from the Bas-Congo region (Democratic Republic of the  
755 Congo) in the frame of regional tentative correlations. *Geol. Belg.* 18, 126-146.  
756
- 757 Clark, D., 1980. The diagenesis of Zechstein carbonate sediments. In: F chtbauer, H., Peryt, T.  
758 (Eds.), *The Zechstein Basin with Emphasis on Carbonate Sequences*. Stuttgart, E.  
759 Schweizerbart’sche Verlagbuchhandlung. *Contrib. to Sedimentol.* 9, 16.  
760
- 761 Chorowitz, J., Le Fournier, J., Mvumbi, M., 1990. La Cuvette Centrale du Za re: un bassin initi  au  
762 Prot rozo ique sup rieur. Contribution de l’analyse du r seau hydrographique. *Comptes-Rendus*  
763 *l’Acad mie des Sci. Paris* 331, 349–356.
- 764 Cisne, J.L., 1986. Earthquakes recorded stratigraphically on carbonate platforms. *Nature* 323, 320–  
765 322. <https://doi.org/10.1038/323320a0>
- 766 Clough, J.G., Goldhammer, R.K., 2000. Evolution of the Neoproterozoic dolomite ramp complex,  
767 Northeastern Brooks range, Alaska. In: Grotzinger, J.P., James, N.P. (Eds.). *Carbonate*  
768 *sedimentation and diagenesis in the evolving Precambrian world*. *Soc. Econ. Paleontol. Mineral.*  
769 *Spec. Publ.* 209–241.  
770
- 771 Dadet, P., 1969. Notice explicative de la carte g ologique de la R publique du Congo Brazzaville au  
772 1/500000. *M moire du Bureau de Recherches G ologiques et Mini res* 40, 103.
- 773 Delhaye, F., Sluys, M., 1923. Esquisse g ologique du Congo occidentale. Etude du syst me Schisto-  
774 Calcaire, missions g ologiques de 1914 et 1918–19. *Etablissement Cartographique E. Patesson,*  
775 *Bruxelles-Uccle*, 1923–1924.
- 776 De Paepe, P., Hertogen, J., Tack, L., 1975. Mise en  vidence de laves en coussins dans les faci s  
777 volcaniques basiques du massif de Kimbundu (Bas-Za re) et implications pour le magmatisme

- 778 Ouest-Congolien 98, 251–270.
- 779 Delpomdor, F., Eyles, N., Tack, L., Pr at, A., 2016. Pre- and post-Marinoan carbonate facies of the  
780 Democratic Republic of the Congo: Glacially- or tectonically-influenced deep-water sediments?  
781 *Palaeogeogr. Palaeoclimatol. Palaeoecol.* 457, 144–157.  
782 <https://doi.org/10.1016/J.PALAEO.2016.06.014>
- 783 Delpomdor, F., Tack, L., Cailteux, J., Pr at, A., 2015. The C2 and C3 formations of the Schisto-  
784 Calcaire Group (West Congolian Supergroup) in the Democratic Republic of the Congo: an example  
785 of Post-Marinoan sea level fluctuations as a result of extensional tectonisms. *J. Afr. Earth Sci.* 110, 14-  
786 33.
- 787
- 788 Delpomdor, F., Pr at, A., 2013a. Early and late neoproterozoic c, o and sr isotope chemostratigraphy  
789 in the carbonates of west congo and mbuji-mayi supergroups: A preserved marine signature?  
790 *Palaeogeogr. Palaeoclimatol. Palaeoecol.* 389, 35–47.  
791 <https://doi.org/10.1016/j.palaeo.2013.07.007>
- 792 Delpomdor, F., Pr at, A., 2013b. Early and late Neoproterozoic C, O and Sr isotope  
793 chemostratigraphy in the carbonates of West Congo and Mbuji-Mayi supergroups: A preserved  
794 marine signature? *Palaeogeogr. Palaeoclimatol. Palaeoecol.* 389, 35–47.  
795 <https://doi.org/10.1016/J.PALAEO.2013.07.007>
- 796 Delpomdor, F., Van Vliet, N., Devleeschouwer, X., Tack, L., Pr at, A., 2018. Evolution and estimated  
797 age of the C5 Lukala carbonate-evaporite ramp complex in the Lower Congo region (Democratic  
798 Republic of Congo): New perspectives in Central Africa. *J. African Earth Sci.* 137, 261–277.  
799 <https://doi.org/10.1016/J.JAFREARSCI.2017.10.021>
- 800 Delpomdor, R.A., 2017. Facies and micromorphology of the Neoproterozoic Upper Diamictite  
801 Formation in the Democratic Republic of Congo : new evidence of sediment gravity flow.  
802
- 803 Deynoux, M., Affaton, P., Trompette, R., Villeneuve, M., 2006. Pan-African tectonic evolution and  
804 glacial events registered in Neoproterozoic to Cambrian cratonic and foreland basins of West  
805 Africa. *J. Afr. Earth Sci.* 46, 397–426.
- 806 Dill, R.F., Shinn, E.A., Jones, A.T., Kelly, K., Steinen, R.P., 1986. Giant subtidal stromatolites

- 807 forming in normal salinity waters. *Nature* 324, 55–58. <https://doi.org/10.1038/324055a0>
- 808 Direen, N.G., Jago, J.B., 2008. The Cottons Breccia (Ediacaran) and its tectonostratigraphic context  
809 within the Grassy Group, King Island, Australia: A rift-related gravity slump deposit.  
810 *Precambrian Res.* 165, 1–14. <https://doi.org/10.1016/J.PRECAMRES.2008.05.008>
- 811 Dott, R.H., Bourgeois, J., 1982. Hummocky stratification: Significance of its variable bedding  
812 sequences. *Geol. Soc. Am. Bull.* 93, 663. [https://doi.org/10.1130/0016-](https://doi.org/10.1130/0016-7606(1982)93<663:HSSOIV>2.0.CO;2)  
813 [7606\(1982\)93<663:HSSOIV>2.0.CO;2](https://doi.org/10.1130/0016-7606(1982)93<663:HSSOIV>2.0.CO;2)
- 814 Duke, W.L., 1985. Hummocky cross-stratification, tropical hurricanes, and intense winter storms.  
815 *Sedimentology* 32, 167–194. <https://doi.org/10.1111/j.1365-3091.1985.tb00502.x>
- 816 Dumas, S., Arnott, R.W.C., 2006. Origin of hummocky and swaley cross-stratification— The  
817 controlling influence of unidirectional current strength and aggradation rate. *Geology* 34, 1073.  
818 <https://doi.org/10.1130/G22930A.1>
- 819 Dunham, R.J., 1962. Classification of Carbonate Rocks According to Depositional Textures 38, 108–  
820 121.
- 821 Elrick, M., 1995. Cyclostratigraphy of Middle Devonian Carbonates of the Eastern Great Basin,  
822 *Journal of Sedimentary Research, SEPM* 65 (1), 61–67
- 823 Embry, A.F., Klovan, J.E., 1972. Absolute water depth limits of Late Devonian paleoecological zones.  
824 *Geol. Rundschau* 61, 672–686. <https://doi.org/10.1007/BF01896340>
- 825
- 826 Enos, P., 1983. Shelf Environment: Chapter 6. *Amer. Ass. Pet. Geol. Stud. Geol.* 43, 267–295.  
827
- 828 Eyles, N., Januszczak, N., 2004. “Zipper-rift”: a tectonic model for Neoproterozoic glaciations during  
829 the breakup of Rodinia after 750 Ma. *Earth-Science Rev.* 65, 1–73.  
830 [https://doi.org/10.1016/S0012-8252\(03\)00080-1](https://doi.org/10.1016/S0012-8252(03)00080-1)
- 831 Flügel, E., 2004. *Microfacies of Carbonate Rocks. Analysis, Interpretation and Application*, Berlin,  
832 Heidelberg, New York: Springer-Verlag. Cambridge University Press.  
833 <https://doi.org/10.1017/S0016756806221940>
- 834 Frimmel, H.E., Tack, L., Basei, M.S., Nutman, A.P., Boven, A., 2006. Provenance and

- 835 chemostratigraphy of the Neoproterozoic West Congolian Group in the Democratic Republic of  
836 Congo. *J. African Earth Sci.* 46, 221–239. <https://doi.org/10.1016/j.jafrearsci.2006.04.010>
- 837 Ginsburg, R.N., 1971. Landward Movement of Carbonate Mud: New Model for Regressive Cycles in  
838 Carbonates. *Amer. Ass. Pet. Geol. Stud. Geol.* 55 (2), 340. [https://doi.org/10.1306/5D25CE81-  
839 16C1-11D7-8645000102C1865D](https://doi.org/10.1306/5D25CE81-16C1-11D7-8645000102C1865D)
- 840 Glumac, B., Walker, K.R., 2000. Carbonate Deposition and Sequence Stratigraphy of the Terminal  
841 Cambrian Grand Cycle in the Southern Appalachians, U.S.A. *J. Sediment. Res.* 70, 952–963.  
842 <https://doi.org/10.1306/2DC40943-0E47-11D7-8643000102C1865D>
- 843 Hardie, L.A., 1977. Sedimentation on the Modern Carbonate Tidal Flats of north- west Andros Island,  
844 Bahamas. Johns Hopkins University Press, 202 pp.
- 845 Hoffman, P.F., Kaufman, A.J., Halverson, G.P., Schrag, D.P., 1998. A Neoproterozoic snowball  
846 Earth. *Sciences* 281, 1342-1376.
- 847 Hardie, L.A., Ginsburg, R.N., 1977. Layering; the origin and environmental significance of lamination  
848 and thin bedding. In: *Sedimentation on the Modern Carbonate Tidal Flats of Northwest Andros  
849 Island, Bahamas* (Ed. L.A. Hardie), John Hopkins University, *Stud. Geol* 22, 50–123.
- 850 Hoffman, P.F., Schrag, D.P., 2002. The snowball Earth hypothesis: testing the limits of global change.  
851 *Terra Nov.* 14, 129–155. <https://doi.org/10.1046/j.1365-3121.2002.00408.x>
- 852 James, N.P., Bourque, P.-A., 1992. Reefs and mounds. In: Walker, R.G., James, N.P. (Eds.), *Facies  
853 Models, Response to Sea Level Change*. *Geol. Assoc. Canada* 1, 323–347.
- 854 Kampunzu, A.B., Kapenda, D., Manteka, B., 1991. Basic magmatism and geotectonic evolution of the  
855 Pan African belt in central Africa: Evidence from the Katangan and West Congolian segments.  
856 *Tectonophysics* 190, 363–371. [https://doi.org/10.1016/0040-1951\(91\)90438-X](https://doi.org/10.1016/0040-1951(91)90438-X)
- 857 Keith, B.D., Zuppann, C.W. (eds ), 1993. Mississippian oolites and modern analogs. *Amer. Ass. Pet.  
858 Geol. Stud. Geol.* 35, 265 pp. <https://doi.org/10.1306/St35571>
- 859 Kinsmann, D.J.J., 1969. Modes of formation, sedimentary associations and diagnostic features of  
860 shallow-water and supratidal evaporites. *Bull. Am. Assoc. Petrol. Geol.* 53, 830–840.
- 861
- 862 Kirschvink, J.L., 1992. Late Proterozoic low-latitude global glaciation: the snowball Earth. In: Schopf,

- 863 J.W., Klein, C., (eds), *The Proterozoic biosphere: a multidisciplinary study*. Cambridge  
864 University Press, Cambridge, 51-52.
- 865 Kromkamp, J.C., Perkins, R., Dijkman, N., Consalvey, M., Andres, M., Reid, R.P., 2007. Resistance  
866 to burial of cyanobacteria in stromatolites. *Aquat. Microb. Ecol.* 48, 123–130.  
867 <https://doi.org/10.3354/ame048123>
- 868 Lepersonne, J., 1974. Carte géologique à l'échelle 1/200000. Notice explicative de la feuille Ngungu  
869 (Degré carré S6/14 = SB 33.9). République Démocratique du Congo. Département des Mines,  
870 Direction du Service Géologique, 61 pp.
- 871 Li, Z.X., Bogdanova, S.V., Collins, A.S., Davidson, A., De Waele, B., Ernst, R.E., Fitsimons, I.C.W.,  
872 Fuck, R.A., Gladkochub, D.P., Jacobs, J., Karlstom, K.E., Lu, S., Natapov, L.M., Pease, V.,  
873 Pisarevsky, S.A., Thrane, K., Vernikovskiy, V., 2008. Assembly, configuration, and break-up  
874 history of Rodinia: a synthesis. *Precambrian Research* 160 (1–2), 179–210.
- 875
- 876 Mamet, B., Prétat, A., 2005. Sédimentologie de la série viséenne d'Avesnes-sur-Helpe (Avesnois,  
877 Nord de la France). *Geol. Belgica* 8, 91–107.
- 878 Monié, P., Bosch, D., Bruguier, O., Vauchez, A., Rolland, Y., Nsungani, P., Buta, N.A., 2012. The  
879 late Neoproterozoic/early palaeozoic evolution of the West Congo belt of NW Angola:  
880 geochronological (UPb and Ar-Ar) and petrostructural constraints. *Terra Nova* 24 (3), 1-10.
- 881
- 882 Morsilli, M., Pomar, L., 2012. Internal waves vs. surface storm waves: a review on the origin of  
883 hummocky cross-stratification. *Terra Nov.* 24, 273–282. [https://doi.org/10.1111/j.1365-](https://doi.org/10.1111/j.1365-3121.2012.01070.x)  
884 [3121.2012.01070.x](https://doi.org/10.1111/j.1365-3121.2012.01070.x)
- 885 Muanza-Kant, P., Mpiana, Ch, Kanda-Nkula, V., Tack, L., Baudet, D., Archibald, D.B., Glorie, S.,  
886 2016. The lower Diamictite Formation of the Cataractes Group, West Congo Supergroup (Bas-  
887 Congo, DRC): a 700 Ma marker of extensional episodic activity during breakup of Columbia.,  
888 in: 5th International Geologica Belgica 2016 Congress, 26-29 January 2016. University of Mons,  
889 Mons, Belgium, P. 57. Abstract Book.
- 890 Noffke, N., 2010. *Geobiology: Microbial mats in sandy deposits from the Archean era to today*.  
891 Springer. <https://doi.org/10.1007/978-3-642-12772-4>

- 892 Noffke, N., 2000. Extensive microbial mats and their influences on the erosional and depositional  
893 dynamics of a siliciclastic cold water environment (Lower Arenigian, Montagne Noire, France).  
894 *Sediment. Geol.* 136, 207–215. [https://doi.org/10.1016/S0037-0738\(00\)00098-1](https://doi.org/10.1016/S0037-0738(00)00098-1)
- 895 Patterson, R.J., Kinsman, D.J.J., 1981. Hydrologic Framework of a Sabkha Along Arabian Gulf. *Am.*  
896 *Assoc. Pet. Geol. Bull.* 65, 1457–1475.
- 897
- 898 Pedersen, G.K., 1985. Thin, fine-grained storm layers in a muddy shelf sequence: an example from the  
899 Lower Jurassic in the Stenlille 1 well, Denmark. *J. Geol. Soc. London.* 142, 357–374.  
900 <https://doi.org/10.1144/gsjgs.142.2.0357>
- 901 Pedrosa-Soares, A.C., Alkmim, F.F., Tack, L., Noce, C.M., Babinski, M., Silva, L.C., Martins-Neto,  
902 M.A., 2008. Similarities and differences between the Brazilian and African counterparts of the  
903 Neoproterozoic Araçuaí-West Congo orogen. *Geol. Soc. London, Spec. Publ.* 294, 153–172.  
904 <https://doi.org/10.1144/SP294.9>
- 905 Pedrosa-Soares, A.C., Alkmim, F.F., 2011. How many rifting events preceded the develop- ment of the  
906 Araçuaí–West Congo orogen? *Geonomos* 19 (2), 244–251.
- 907 Pedrosa-Soares, A.C., Babinski, M., Noce, C., Martins, M., Queiroga, G., Vilela, F., 2011. Chapter 49  
908 The Neoproterozoic Macaúbas Group, Araçuaí orogen, SE Brazil. *Geol. Soc. London, Mem.* 36,  
909 523–534. <https://doi.org/10.1144/M36.49>
- 910 Perkins, R.G., Kromkamp, J.C., Pamela Reid, R., 2007. Importance of light and oxygen for  
911 photochemical reactivation in photosynthetic stromatolite communities after natural sand burial.  
912 *Mar. Ecol. Prog. Ser.* 349, 23–32. <https://doi.org/10.3354/meps07087>
- 913 Poidevin, J.L., 2007. Stratigraphie isotopique du strontium et datation des formations carbonatées et  
914 glaciogéniques néoproterozoïques du Nord et de l’Ouest du craton du Congo. *Comptes Rendus -*  
915 *Geosci.* 339, 259–273. <https://doi.org/10.1016/j.crte.2007.02.007>
- 916 Préat, A., Delpomdor, F., Ackouala Mfere, A.P., Callec, Y., 2018. Paleoenvironments,  $\delta^{13}\text{C}$  and  $\delta^{18}\text{O}$   
917 signatures in the Neoproterozoic carbonates of the Comba Basin, Republic of Congo:  
918 Implications for regional correlations and Marinoan event. *J. African Earth Sci.* 137, 69–90.  
919 <https://doi.org/10.1016/j.jafrearsci.2017.09.002>

- 920 Pr at, A., Kolo, K., Prian, J.-P., Delpomdor, F., 2010. A peritidal evaporite environment in the  
921 Neoproterozoic of South Gabon (Schisto-Calcaire Subgroup, Nyanga Basin). *Precambrian Res.*  
922 177, 253–265. <https://doi.org/10.1016/J.PRECAMRES.2009.12.003>
- 923 Pr at, A.R., Delpomdor, F., Kolo, K., Gillan, D.C., Prian, J.-P., 2011. Stromatolites and  
924 Cyanobacterial Mats in Peritidal Evaporative Environments in the Neoproterozoic of Bas-Congo  
925 (Democratic Republic of Congo) and South Gabon. Springer, Dordrecht, pp. 43–63.  
926 [https://doi.org/10.1007/978-94-007-0397-1\\_3](https://doi.org/10.1007/978-94-007-0397-1_3)
- 927 Sarkar, S., Bose, P.K., 1992. Variations in Late Proterozoic stromatolites over a transition from basin  
928 plain to nearshore subtidal zone. *Precambrian Res.* 56, 139–157. [https://doi.org/10.1016/0301-](https://doi.org/10.1016/0301-9268(92)90088-6)  
929 [9268\(92\)90088-6](https://doi.org/10.1016/0301-9268(92)90088-6)
- 930 Satterley, A.K., 1996. The interpretation of cyclic successions of the Middle and Upper Triassic of the  
931 Northern and Southern Alps. *Earth-Science Rev.* 40, 181–207. [https://doi.org/10.1016/0012-](https://doi.org/10.1016/0012-8252(95)00063-1)  
932 [8252\(95\)00063-1](https://doi.org/10.1016/0012-8252(95)00063-1)
- 933
- 934 Scholle, P.A., Kinsman, D.J.J., 1974. Aragonitic and High-Mg Calcite Caliche from the Persian Gulf--  
935 A Modern Analog for the Permian of Texas and New Mexico. *J. Sediment. Res.* 44, 904–916.  
936 <https://doi.org/10.1306/212F6BD6-2B24-11D7-8648000102C1865D>
- 937
- 938 Sellwood, B.W., 1986. Shallow-marine carbonate environments. In: H.G. Reading (Editor),  
939 *Sedimentary Environments and Facies*. Blackwell, 2nd ed. 283–342.
- 940
- 941 Shearman, D.J., 1963. Recent anhydrite, gypsum, dolomite and halite from the coastal flat of the  
942 Arabian shore of the Persian Gulf. *Proc. Geol. Soc. Lond.* 1607/63, 5
- 943
- 944 Schermerhorn, L.J.G., Stanton, W.I., 1963. Tilloids in the West Congo geosyncline. *Q. J. Geol. Soc.*  
945 119, 201–241. <https://doi.org/10.1144/gsjgs.119.1.0201>
- 946
- 947 Shukla, V., Friedman, G.M., 1981. An unusual occurrence of surficial anhydrite in a moist temperate  
948 zone: Example from the Lockport Formation (Middle Silurian) of New York. *Sediment. Geol.*  
949 29, 125–131. [https://doi.org/10.1016/0037-0738\(81\)90003-8](https://doi.org/10.1016/0037-0738(81)90003-8)

- 950 Sibley, D.F., Gregg, J., 1987. Classification of Dolomite Rock Textures. *J. Sediment. Res.* Vol. 57,  
951 967–975. <https://doi.org/10.1306/212F8CBA-2B24-11D7-8648000102C1865D>
- 952 Sikorski, J., 1958. Echelle stratigraphique provisoire des étages C1-C2-C3 du système Schisto-  
953 Calcaire du Bas-Congo. *CIMINGA*, note n°15.
- 954 Straathof, G.B., 2011. Neoproterozoic low latitude glaciations: an african perspective. The University  
955 of Edinburgh.
- 956 Strasser, A., 2016. Hiatuses and condensation: an estimation of time lost on a shallow carbonate  
957 platform. *Depos. Rec.* 1, 91–117. <https://doi.org/10.1002/dep2.9>
- 958 Strasser, A., 1991. Lagoonal-peritidal sequences in carbonate environments: autocyclic and allocyclic  
959 processes. In: Einsele G, Ricken W, Seilacher A (Eds), *Cycles and events in stratigraphy*.  
960 Springer, Berlin, 709–721.
- 961 Tack, L., Wingate, M.T., Liégeois, J.-P., Fernandez-Alonso, M., Deblond, A., 2001. Early  
962 Neoproterozoic magmatism (1000–910 Ma) of the Zadinian and Mayumbian Groups (Bas-  
963 Congo): onset of Rodinia rifting at the western edge of the Congo craton. *Precambrian Res.* 110,  
964 277–306. [https://doi.org/10.1016/S0301-9268\(01\)00192-9](https://doi.org/10.1016/S0301-9268(01)00192-9)
- 965
- 966 Tack, L., De Grave, J., Burgess, R., Baudet, D., Fernandez-Alonso, M., Kongota-Isasi, E., Nseka-  
967 Mbemba, P., Delvaux, D., 2018. 525 Ma riebeckite in a quartz vein into the Noqui granite: evidence  
968 for a late Pan African extensional event in the West Congo Belt (Matadi area, Bas-Congo region, DR  
969 Congo). 17<sup>th</sup> Conference of the Geological Society of Africa and 27<sup>th</sup> Colloquium of African  
970 Geology. Aveiro, Portugal.
- 971
- 972 Tait, J., Delpomdor, F., Preat, A., Tack, L., Straathof, G., Nkula, V.K., 2011. Chapter 13  
973 Neoproterozoic sequences of the West Congo and Lindi/Ubangi Supergroups in the Congo  
974 Craton, Central Africa. *Geol. Soc. London, Mem.* 36, 185–194. <https://doi.org/10.1144/M36.13>
- 975 Thiéblemont, D., Castaing, C., Billa, M., Bouton, P., Préat, A., 2009. Notice explicative de la carte  
976 géologique et des ressources minérales de la République Gabonaise à 1/1000000. Program.  
977 Sysmin 8 ACP GA 017 384pp.
- 978 Trompette, R., Boudzoumou, F., 1988. Palaeogeographic significance of stromatolitic buildups on

- 979 Late Proterozoic platforms: The example of the West Congo basin. *Palaeogeogr. Palaeoclimatol.*  
 980 *Palaeoecol.* 66, 101–112. [https://doi.org/10.1016/0031-0182\(88\)90083-1](https://doi.org/10.1016/0031-0182(88)90083-1)
- 981 Tucker, M.E., Wright, V.P., Dickson, J.A.D., Wiley InterScience (Online service), 1990. Carbonate  
 982 sedimentology. Blackwell Scientific Publications.
- 983 Tucker, M.E., Wright, V.P., 1990. Carbonate Sedimentology. Blackwell Scientific Publications,  
 984 Oxford, 482 pp.
- 985  
 986 Uhlein, G.J., Uhlein, A., Pereira, E., Caxito, F.A., Okubo, J., Warren, L. V., Sial, A.N., 2019.  
 987 Ediacaran paleoenvironmental changes recorded in the mixed carbonate-siliciclastic Bambuí  
 988 Basin, Brazil. *Palaeogeogr. Palaeoclimatol. Palaeoecol.* 517, 39–51.  
 989 <https://doi.org/10.1016/j.palaeo.2018.12.022>
- 990 Walker, R.G. and Plint, A.G., 1992. Wave-and Storm-Dominated Shallow Marine Systems. In:  
 991 Walker, R.G. and James, N.P., Eds., *Facies Models: Response to Sea Level Change*. Geol.  
 992 Assoc. Canada, Newfoundl. 219–238.
- 993 Wang, J., Li, Z.-X., 2003. History of Neoproterozoic rift basins in South China: implications for  
 994 Rodinia break-up. *Precambrian Res.* 122, 141–158. [https://doi.org/10.1016/S0301-](https://doi.org/10.1016/S0301-9268(02)00209-7)  
 995 [9268\(02\)00209-7](https://doi.org/10.1016/S0301-9268(02)00209-7)
- 996  
 997 Young, G.M., 1995. Are Neoproterozoic glacial deposits preserved on the margins of Laurentia  
 998 related to the fragmentation of two supercontinents? *Geology* 23, 153.  
 999 [https://doi.org/10.1130/0091-7613\(1995\)023<0153:ANGDPO>2.3.CO;2](https://doi.org/10.1130/0091-7613(1995)023<0153:ANGDPO>2.3.CO;2)
- 1000  
 1001
- 1002 **Table 1** Location (latitude, longitude and elevation) of the identified outcrops in the studied  
 1003 area. Most of the outcrops have been described in this study. See Fig. 1, Fig. 16 and text for  
 1004 details.
- 1005
- 1006 **Table 2** Summary of facies associations (FA) and facies (F) defined in the SCI<sub>c</sub> Formation with  
 1007 descriptions and environmental interpretations.
- 1008

1009 **Table 3** Cycle features of SCI<sub>c</sub> Formation in the studied area.

1010

1011 **Table 4** Detailed description of D and Saris sections

1012

1013 **Figure 1** Location map of the Neoproterozoic West Congo Basin (NWCB) divided into Niari-Nyanga,

1014 Comba, Lower Congo and North Angola (NA) subbasins. The Niari-Nyanga, Lower Congo and North

1015 Angola subbasins record sedimentation on a passive margin of the Congo Craton, and the Comba

1016 subbasin belongs to the SE margin of the Sangha aulacogen.

1017

1018 **Figure 2** Comparative lithostratigraphy between the West Congolian Supergroup in RC and the West

1019 Congo Supergroup in DRC. In RC, the stratigraphy of the West Congolian Supergroup has been

1020 recently revised by Charles et al. (2015). In DRC, the Lukala Subgroup, formerly Schisto-Calcaire

1021 Subgroup, is divided into five formations (C1 to C5), which are stratigraphically equivalent with the

1022 SCI Formation – correlated with the C1 to C3 formations of Lower Congo subbasin, SCII Formation –

1023 correlated with the C4 Formation of Lower Congo subbasin, and SCIII Formation – correlated with

1024 the C5 Formation of Lower Congo subbasin. Sr is based on worldwide  $^{87}\text{Sr}/^{86}\text{Sr}$  composition of

1025 seawater during the Neoproterozoic (1000-542 Ma) Era.

1026

1027 **Figure 3** Simplified geological map showing location of the identified outcrops (L1, U and T to

1028 Zanzo, V, W and X from East to West). No sections have been described for A, E, L1, U, V, W, X and

1029 Y in this study. See Fig. 16 for description of each section.

1030

1031 **Figure 4** Field and thin-section photographs of homogeneous clayey mudstones and laminar silty  
1032 mudstones (F1) in the SCI<sub>c</sub> Formation. **(A)** Alternations of darker and purplish layers consisting of  
1033 clayey silty carbonates and microbial mudstones overlain by a domal stromatolite (in the background).  
1034 The domal stromatolite represents the lower part of a complex zone of giant stromatolites (15-20 m in  
1035 height), section D. **(B, C, D)** Planar and undulating platy limestones (3-5 cm-thick) showing  
1036 alternations of homogeneous carbonate muds and slightly laminar silty mudstones identified as MISS  
1037 (Microbial Induced Sedimentary Structures) by petrographic description, D and O sections. **(E)**  
1038 Microbial mats (dark laminations or MISS undulating levels) within a fine microsparitic matrix.  
1039 Quartz, feldspars and pyrite are recognized within the matrix or overlie the microbial mats, section D.  
1040 **(F)** Dark bacterial filament in a microsparitic matrix, section D.

1041  
1042 **Figure 5** Field photographs of the stromatolitic facies (F2 and F6) in the SCI<sub>c</sub> Formation. **(A)** Upper  
1043 part of a giant domal stromatolite with 4-5 m in width, section H. **(B)** Columnar stromatolite with  
1044 parallel columns, section P. **(C)** Centimetric alternations of grey planar microbial mats and  
1045 accumulations of coarse-grained stromatoclasts forming radial-bundles, section F. **(D)** Giant “cigare”  
1046 or coned-shaped stromatolite (10- 15 m in length), section F . **(E)** Wavy and planar microbial mats,  
1047 section M . **(F)** Small domal stromatolite overlying or laterally relayed by planar microbial mats,  
1048 section D. **(G)** Succession of domal stromatolites in the top of a stromatolitic bioherm (15-20 m in  
1049 height), section H.

1050  
1051 **Figure 6** Sedimentary features of the oolite grainstones in the SCI<sub>c</sub> Formation. **(A)** Bidirectional low-  
1052 angle planar laminations with low-angle truncations, section I. **(B)** Sets of trough-stratifications,

1053 section I. **(C)** Mega-ripples, cross-laminations showing herringbone stratifications, section C. **(D)**  
1054 Mega-ripples showing hummocks and swales with low-angle laminations, section C. **(E)** Mega-ripples  
1055 with hummocks (see arrow) showing SCS when the top of the hummocks has been eroded. Stylolites  
1056 (lower part of the picture) are well developed, with high amplitude, as is generally the case in all the  
1057 oolitic grainstones, section I. **(F, G)** HCS with furrows showing flat (less) and hollow (more) bottoms  
1058 passing in the upper part to mega-ripples (cross-laminations), section S. **(H)** Oolite grainstones (F3a)  
1059 overlying columnar stromatolites (F2), irregular contact between F3a and F2 with thick oolite beds  
1060 overlying giant stromatolite, section T.

1061

1062 **Figure 7** Thin-section and field photographs of the oolitic grainstones-floatstones (F3a and F3b) in the  
1063 SCI<sub>c</sub> Formation. **(A)** Grainstone showing well-sorted spherical oolites (F3a) with both concentric and  
1064 radial structures. Cementation consists of isopachous lamellar calcite and blocky calcite, section  
1065 MAD8017. **(B)** Well represented cementation filling the intergranular porosity in an oolite grainstone  
1066 (F3a). As described later, the cementation consists of isopachous lamellar calcite and a blocky calcite,  
1067 section MAD8018. **(C)** Asymmetric oolite with a concentric cortex and coarse-grained slightly  
1068 rosette-like nuclei, section I. **(D)** Greyish floatstone with dominant aggregates, see (F) for facies  
1069 description, section MAD8018. **(E)** Part of centimetric grapestone in a floatstone ooid-aggregate  
1070 (F3b), the grapestone consists of micritized ooids bounded together by a microsparitic matrix, section  
1071 I. **(F)** Millimetric aggregates in a floatstone or 'false' rudstone, see (D) for the field photograph,  
1072 section I. **(G)** Asymmetric oolites (see black arrows) in a grainstone with equant calcite, section  
1073 MAD8017. **(H)** Asymmetric oolite (see black arrow) in a grapestone. The asymmetric oolite appears  
1074 to be reworked before bounded with other oolites to build the grapestone, as shown by the orientation,

1075 section MAD8017.

1076

1077 **Figure 8** Thin-section and field photographs of lagoonal facies (F3c) and intraformational

1078 conglomerate (F4) in the SCI<sub>c</sub> Formation. **(A)** Peloidal grainstone-packstone with micritic oolites and

1079 relics of larger oolites exhibiting a fine concentric structure in the outer part of the cortex, section

1080 MAD8018. **(B)** Peloidal packstone without micritic oolites or larger concentric oolites as described

1081 previously, section MAD8018. **(C and E)** Homogeneous mudstone with pyrite and oxidized organic

1082 matter relics (see arrow in C), section MAD8016. **(D)** Succession of centimetric beds of greyish

1083 homogeneous mudstones, section MAD8019. **(F)** Peloidal grainstone showing herringbone cross-

1084 stratifications, top of Saris Section (MAD8017). **(G)** Intraformational conglomerate showing

1085 elongated mud-clasts and oolites relics with vadose cementation, section B. **(H)** Intraformational

1086 conglomerate with plurimillimetric and inframillimetric mud-clasts. The larger ones are elongated and

1087 affected by vertical cracks, section MAD8017.

1088

1089 **Figure 9** Thin-section and field photographs of peritidal facies (F3d, F4 and F6) in the SCI<sub>c</sub>

1090 Formation. **(A)** Reddish floatstone with abundant pisoids, Sonocc section. See **(B)** and **(C)** for the

1091 microfacies description. **(B, C)** Plurimillimetric pisoids showing a fine concentric structure, the

1092 nucleus is micritic and partly replaced by a coarse calcite **(B)** and consists of oolites **(C)**. **(D)**

1093 Millimetric asymmetric oolites oriented in opposite directions in a pisoid floatstone. The asymmetric

1094 oolites show a concentric cortex with a coarse granular calcite nucleus, Sonocc section. **(E)**

1095 Inframillimetric alternations of planar microbial mats and peloid packstone. Note that peloids (in the

1096 lower part) show circular cracks, Sonocc section. **(F)** Calcitized anhydrite rosette in a peloidal

1097 bindstone, MAD8017 section. **(G)** Parts of centimetric mud-clasts interlayered by microbial mats

1098 relics, MAD8017 section. **(H)** Spiny (left) and half-moon oolites (right) in a floatstone

1099 intraformational conglomerate with abundant micritic oolites, MAD8017 section.

1100

1101 **Figure 10** Thin-section and field photographs of the fine-grained laminar detrital mudstones (F5) in

1102 the SCI<sub>c</sub> Formation. **(A)** Pluricentimetric alternations of grey-light oolite grainstones (F3a) and fine-

1103 grained laminar detrital mudstones (F5), section F. **(B)** Fine-grained laminar detrital mudstones (F5)

1104 topped by a brecciated bindstone microbial mats (F6) showing random stromatoclasts building slightly

1105 radial bundles structures, section J. **(C)** Thin low-angle light-colored laminae (silty fine sand to fine

1106 silt) interlayered by dark-colored laminae. Light-colored laminae are enriched in quartz, feldspars,

1107 clays minerals, calcite and dolomite crystals (see D). Dark-colored laminae display a pyrite-rich

1108 homogeneous mudstone, section F. **(D)** Quartz, feldspars, clinochlore (greenish crystal), pyrite and

1109 xeno-to hypidiotopic calcite and dolomite crystals in a light-colored laminae of F5, section F.

1110

1111 **Figure 11** Thin section and field photographs of the evaporative dolomudstones (F7) in the SCI<sub>c</sub>

1112 Formation. **(A, B and C)** Reddish and yellowish dolomudstone with abundant rosettes and laths of

1113 evaporative minerals, top of Sonocc section. See Figs. D to G for the microfacies description. **(D and**

1114 **E)** Rosettes and laths of anhydrite now calcitized, the matrix is a slightly microsparitized

1115 dolomudstone. **(F)** Nodule of well-preserved anhydrite partly silicified. **(G)** Evaporative

1116 dolomudstone showing abundant fenestrae testifying vadose conditions.

1117

1118 **Figure 12** Revised sedimentary model of the SCI<sub>c</sub> Formation in the Niari-Nyanga and Comba  
1119 sections of the NWCB in RC from outer-ramp with MISS (FA1) to supratidal sabkha (FA5).  
1120 Facies associations (FA1 to FA5) represent the standard sequence of the studied formation  
1121 (see Table 2 for explanation). The previous sedimentary model has been described in Pr  at et  
1122 al. (2018).

1123  
1124 **Figure 13** Types of cycles (D vs S) with their facies (F1-F7) successions in the SCI<sub>c</sub>  
1125 Formation, showing shallowing upward trends. 'D4 is for 'Deep cycles', 'S' is for Shallow  
1126 cycles'. See Table 3 for explanation

1127  
1128 **Figure 14** Stratigraphic section of the active Saris (MAD8017) quarry exposing the SCI<sub>c</sub> Formation,  
1129 showing sample location (8017-1 to 8017-22), lithologic curve (from F1 to F7 facies),  
1130 sedimentological features and stacking patterns. Explanations in text, for location see Fig. 1. FAS=  
1131 facies successions, PSQ= parasequence, PSQS= parasequence set, Prog. = progradation, Aggr. =  
1132 aggradation. M = mudstone, W = wackestone, P = packstone, G = grainstone, R = rudstone, B =  
1133 boundstone.

1134  
1135 **Figure 15** Stratigraphic section of the inactive D quarry exposing the SCI<sub>c</sub> Formation, sample location  
1136 (D1 to D85), lithologic curve (from F1 to F7 facies), sedimentological features and stacking patterns.  
1137 Explanations in text, for location see Fig. 1. FAS= facies successions, PSQ= parasequence, PSQS=  
1138 parasequence set, Prog. = progradation, Aggr. = aggradation. M = mudstone, W = wackestone, P =  
1139 packstone, G = grainstone, R = rudstone, B = boundstone.

1140

1141

1142 **Figure 16** Stratigraphic correlation of the studied sections based on the stratigraphic key surfaces (TS  
1143 and MFS) and the lithofacies associations. See also Fig. 1 for location of sections T to MAD8019  
1144 (Zanzo). Sections U to Y are not represented here.

1145 TS = transgressive surface represented by a heavy red line, MFS = maximum flooding surface  
1146 represented by a heavy dark line. Filled and unfilled arrows represent respectively complete and  
1147 uncomplete aggradational phases in TST (transgressive system tract) sedimentation. TS =  
1148 transgressive surface, MFS = maximum flooding surface. See text and Fig. 17 for details. Dark  
1149 arrows= aggradation (sections K, H, D, B and Zanzo).

1150

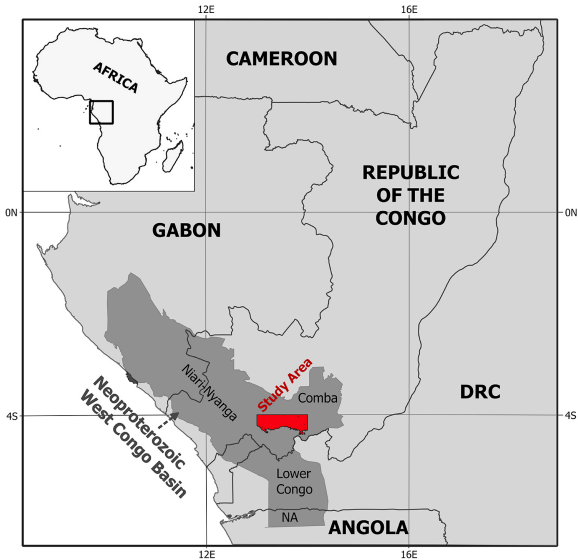
1151 **Figure 17** Tentative sequence stratigraphic correlation of the SCI Subgroup between the  
1152 Niari-Nyanga and Comba subbasins (RC) and Lower Congo subbasin (RDC) with two  
1153 transgressive-regressive third-order sequences. The TST sedimentation is recorded in the  
1154 SC1a and the lower SC1b in RC, and in the C1 Formation and C2a and C2b members in DRC.  
1155 The SC1b in RC, and its stratigraphic coeval C2c to C2e members in DRC is marked by a  
1156 HST phase. The SC1b-SC1c transition is characterized by a LST sedimentation of shallow  
1157 water deposits (FA3/FA4, with abundant S2 cycles), which is also recorded in the C2f to C2h  
1158 members in DRC. The LST phase is topped by a transgressive surface (TS) leading to TST  
1159 sedimentation ('deep' MISS facies) until the maximum flooding surface (MFS) initiating the  
1160 HST sedimentation with giant stromatolites, which are coeval with the C3a Member in DRC.  
1161 The top of the SC1c, and its stratigraphic equivalent C3b Member in DRC, is marked by

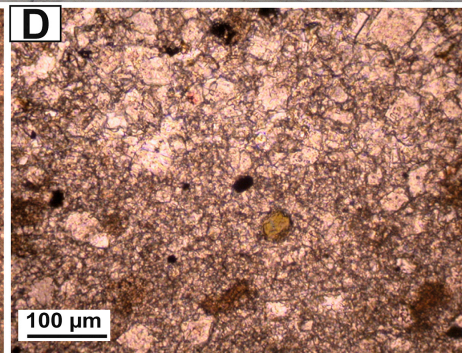
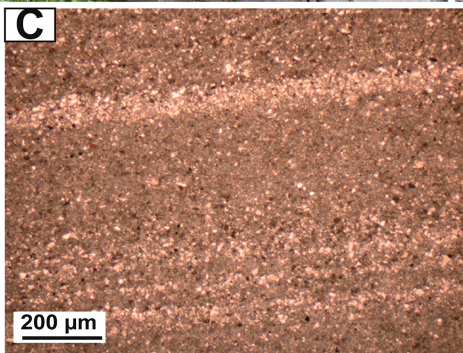
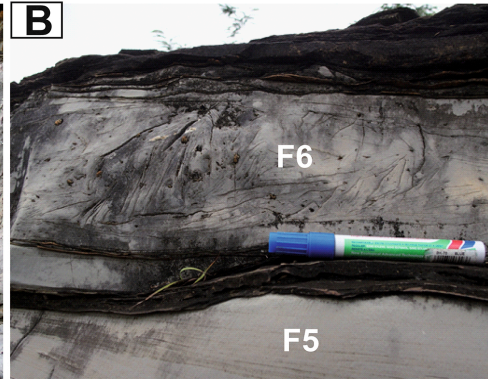
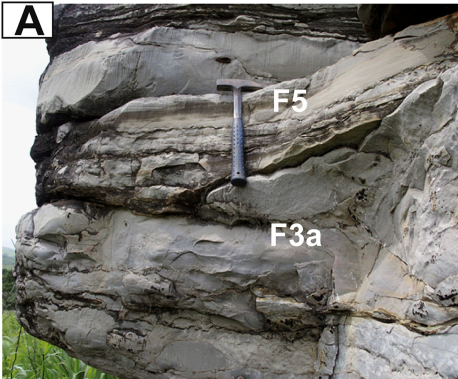
1162 deposition of silty evaporites (LST) at the transition SCI-SCII. TS, MFS and SB (sequence  
1163 boundaries) are indicated respectively by heavy dark and red lines. LST = lowstand system  
1164 tract, TST = transgressive system tract, HST = highstand system tract, FRST= Forced  
1165 regression system tract.

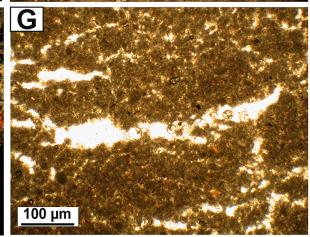
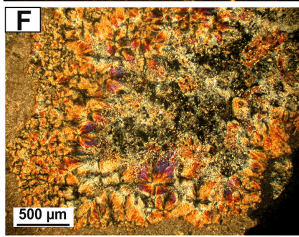
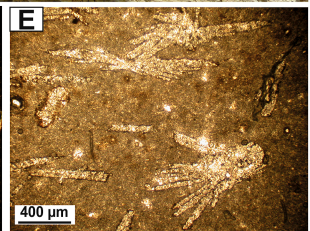
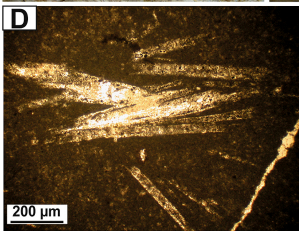
1166

1167

Journal Pre-proof

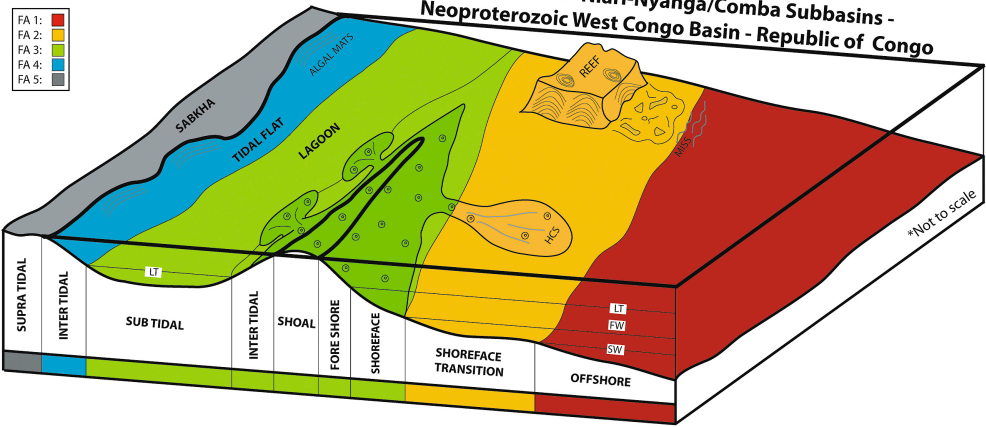






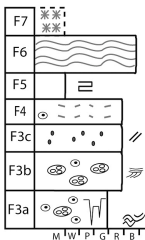
# SC1c Formation - Niari-Nyanga/Comba Subbasins - Neoproterozoic West Congo Basin - Republic of Congo

- FA 1: Red
- FA 2: Yellow
- FA 3: Green
- FA 4: Blue
- FA 5: Grey

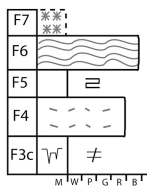


## Peritidal cycles

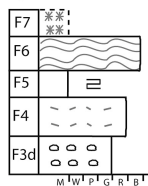
**Cycle S1**



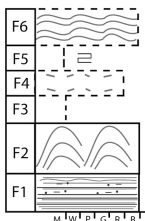
**Cycle S2**



**Cycle S3**

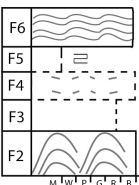


**Cycle D1**



## Deep cycles

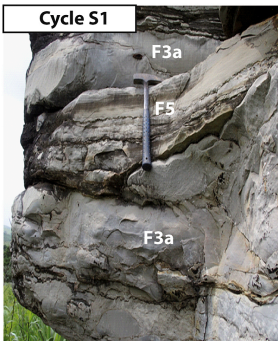
**Cycle D2**



### Legend

- Oolite
- Pisoid
- Peloid / micritic ooid
- ⊕ Aggregate
- ⌒ Domal Stromatolite
- ⌒ Intraformational conglomerate
- ⌒ Planar stromatolite
- ⌒ Evaporite

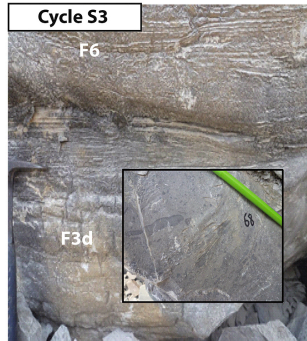
**Cycle S1**



**Cycle S2**



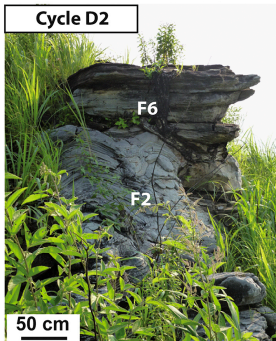
**Cycle S3**



**Cycle D1**

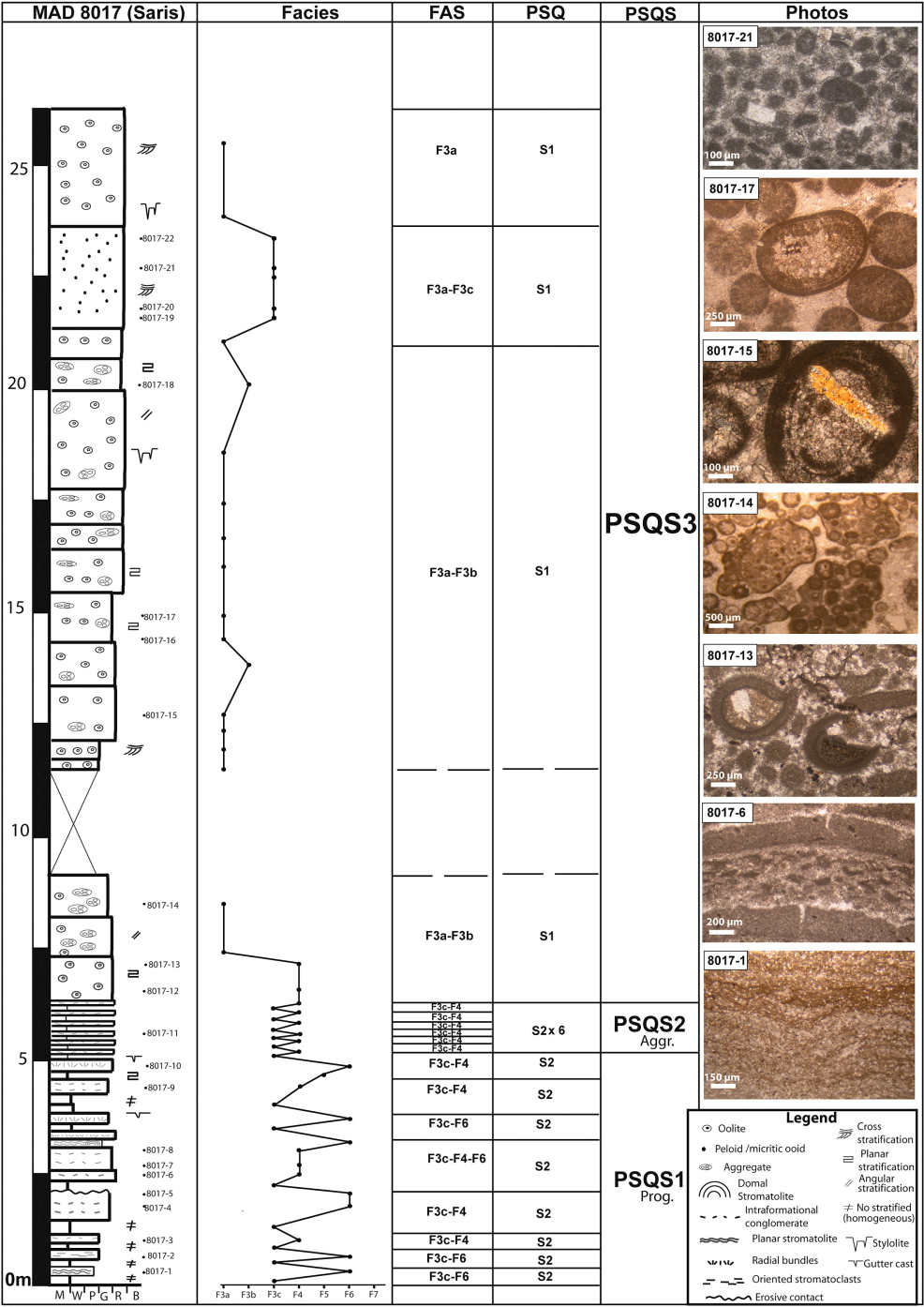


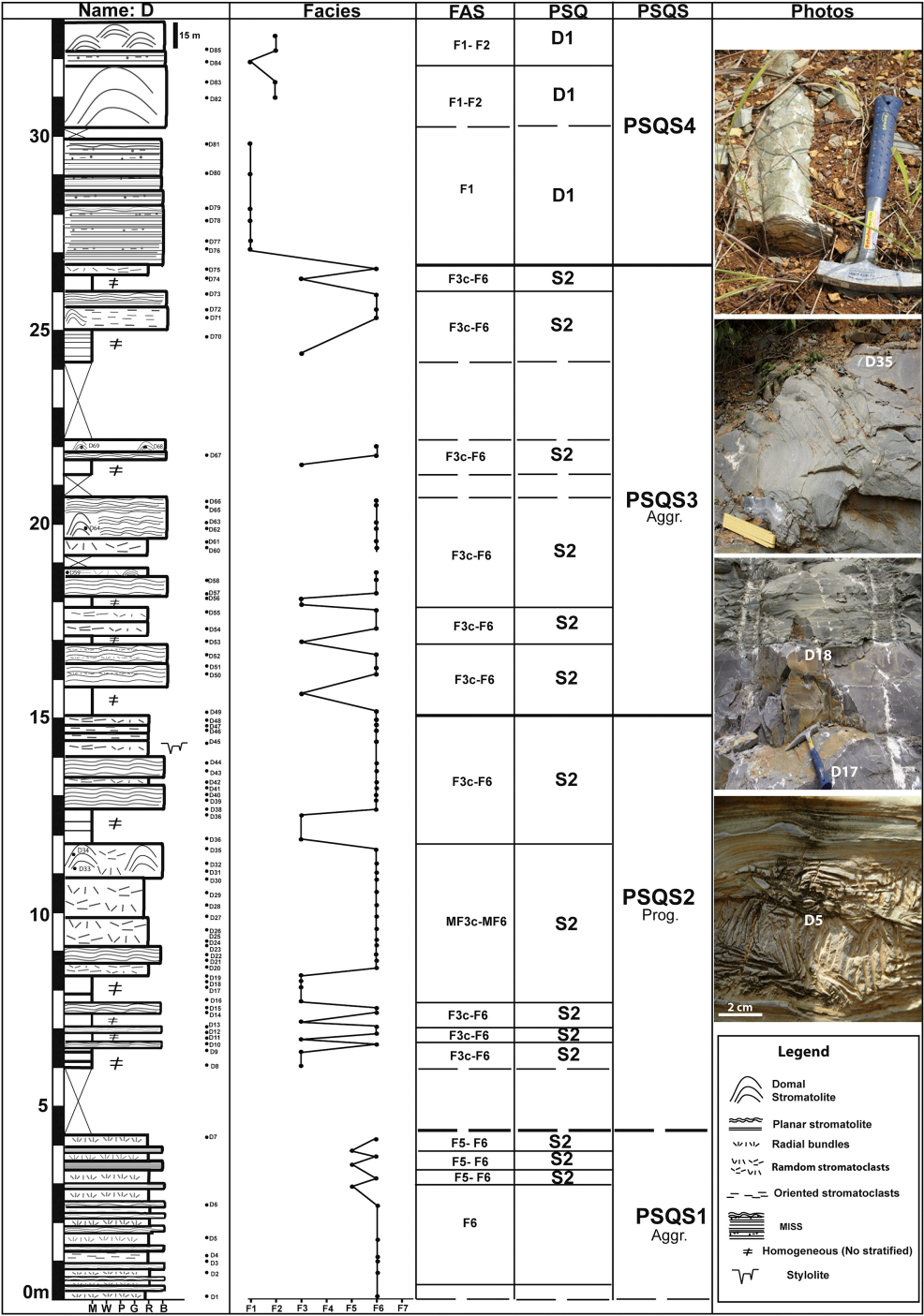
**Cycle D2**

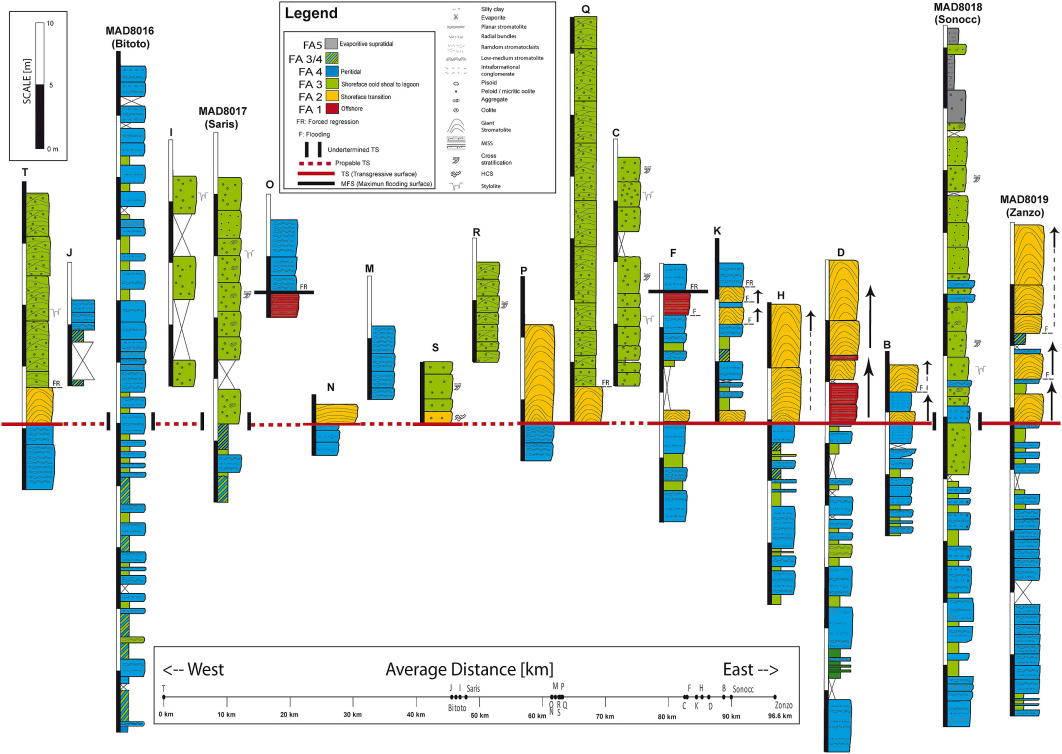


### Legend

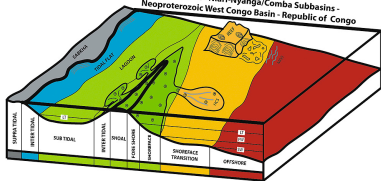
- ⌒ Hummocky cross stratification
- ⌒ Cross stratification
- ≡ Planar stratification
- ≠ No stratified (homogeneous)
- ⌒ Angular stratification
- ⌒ Stylolite



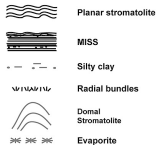




SC1c Formation - Niari-Nyanga/Comba Subbasins - Neoproterozoic West Congo Basin - Republic of Congo

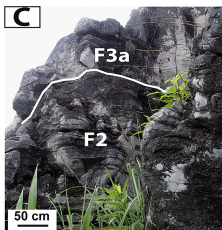


Legend



Formation/Member		Lithology	Third-order sequence
RC	DRC		
SC1la	C4a		LST <sup>TS</sup>
SC1c	C3b		FRST <sup>SB</sup>
	C3a		HST <sup>FRS</sup>
	C2f-C2h		TST <sup>MFS</sup>
			LST <sup>TS</sup>
SC1b	C2c-C2e		HST <sup>SB</sup>
			HST
			HST
	C2a-C2b		TST <sup>MFS</sup>
SC1a	C1		TST

C



B

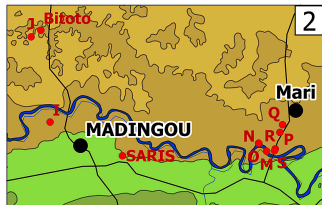
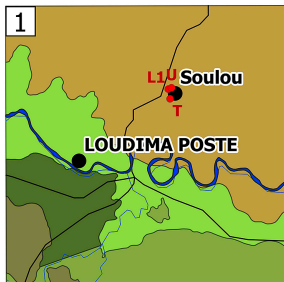
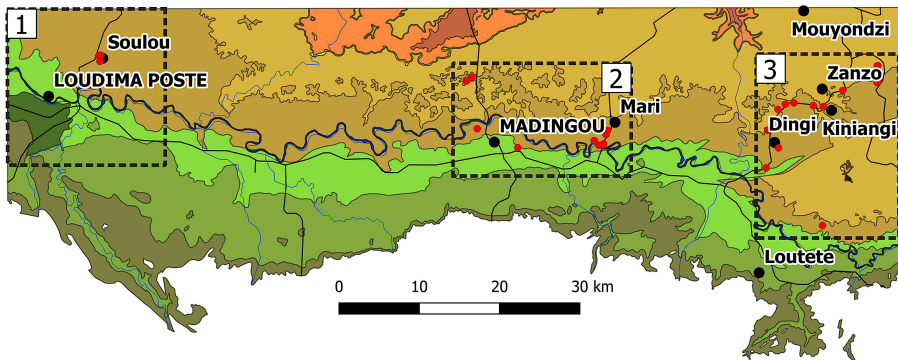


A



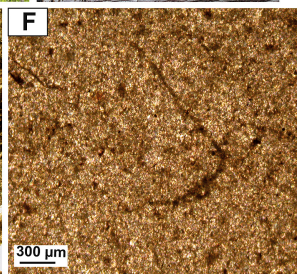
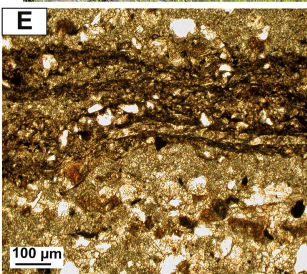
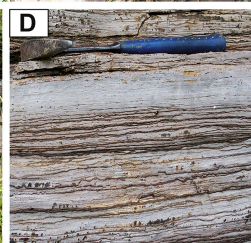
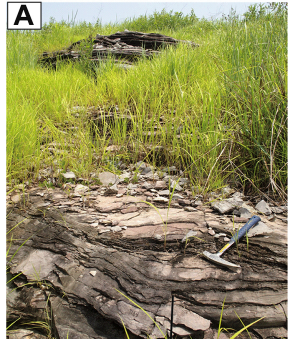
25 m

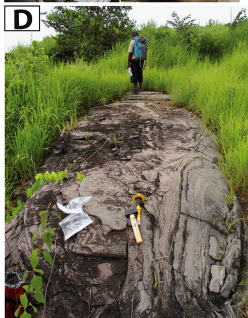


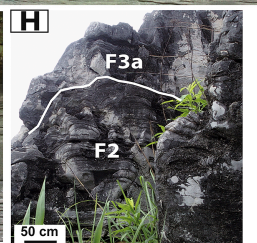


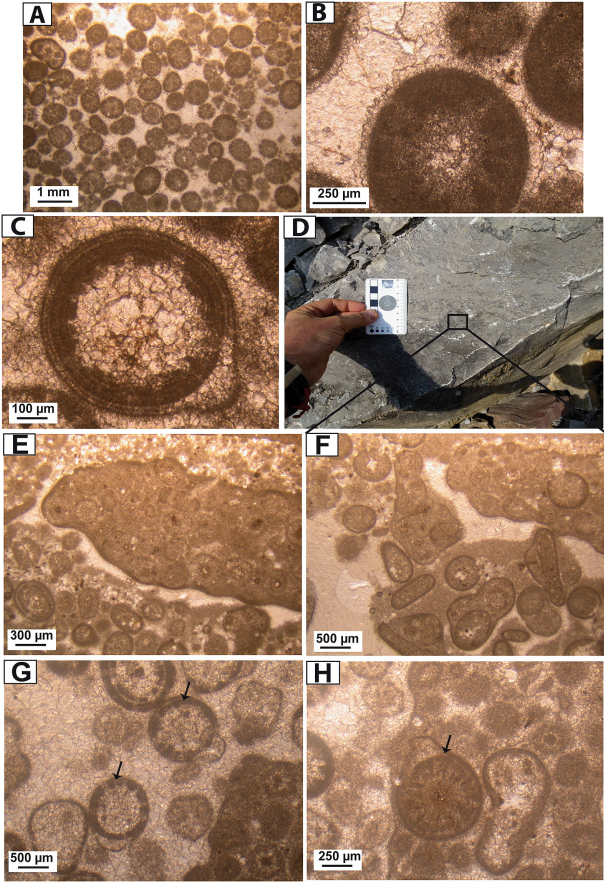
- City
- Outcrop
- Niari river
- River
- Road

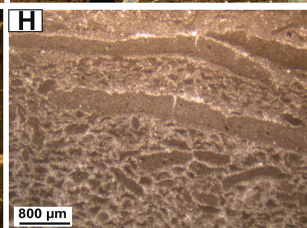
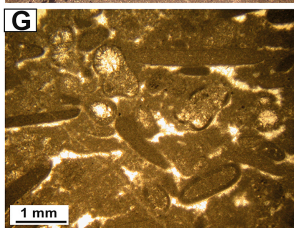
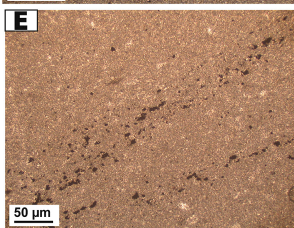
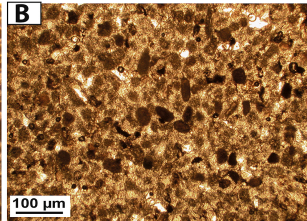
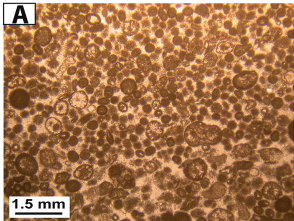
- SCIIc
- SCIIbc
- SCIIb
- SCIIa
- SCIc
- SCIb
- SCIa
- TIN
- Bz

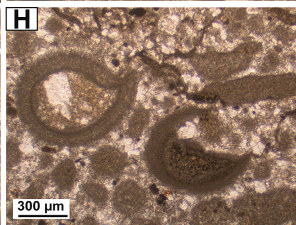
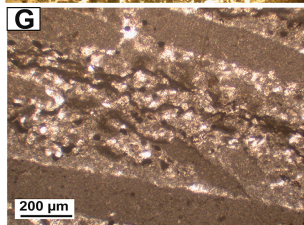
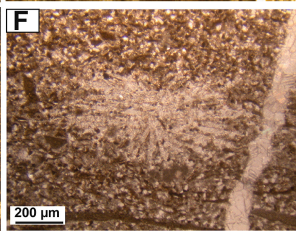
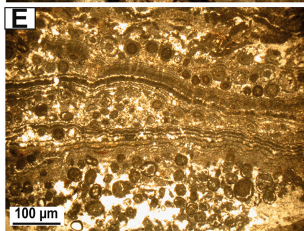
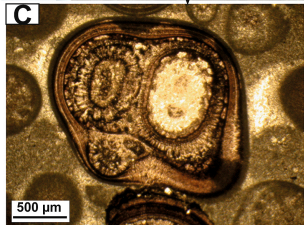
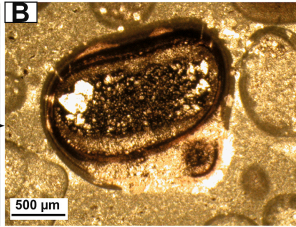
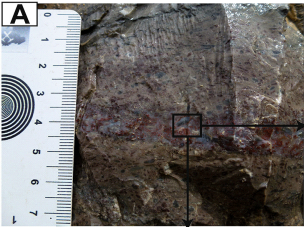












LOG (EPSG:4326 WGS 84)	Latitude	Longitude	Elevation
A	S04°06.687'	E013°54.922'	265m
B	S04°06.621'	E013°54.251'	341m
C	S04°10.824'	E013°51.076'	215m
D	S04°06.436'	E013°52.951'	321m
E	S04°06.874'	E013°51.875'	241m
F	S04°08.285'	E013°51.181'	242m
G	S04°14.720'	E013°54.861'	230m
H	S04°06.517'	E013°52.372'	297m
I	S04°08.150'	E013°31.619'	196m
J	S04°04.922'	E013°30.908'	262m
K	S04°09.470'	E013°51.901'	215 m
L1	S04°03.170'	E013°06.155'	202m
M	S04°09.271'	E013°39.792'	138m
N	S04°08.965'	E013°39.493'	140m
O	S04°08.973'	E013°39.504'	140m
P	S04°08.557'	E013°40.295'	190m
Q	S04°08.266'	E013°40.397'	201m
R	S04°09.180'	E013°40.121'	153m
S	S04°09.252'	E013°40.090'	144m
T	S04°03.540'	E013°06.225'	198m
U	S04°03.119'	E013°06.282'	236m
V	S04°03.931'	E013°58.601'	446m
W	S04°03.933'	E013°58.561'	446m
X	S04°05.066'	E013°58.548'	395m
Y	S04°05.600'	E013°56.229'	371m
MAD8016 (Bitoto)	S04°04.672'	E013°31.278'	268m
MAD8019 (Zanzo)	S04°04.944'	E013°58.648'	370m
MAD8018 (Sonocc)	S04°14.720'	E013°54.861'	230m
MAD8017 (Saris)	S04°09.433'	E013°34.348'	164m

Type	Cycle features
S3	This cycle is relatively rare and less than 1.5 m-thick. The succession consists of pisoidic grainstone/floatstone, intraformational conglomerate, laminar detrital mudstone overlain by laminar microbial mats and evaporitive mudstone with abundant pseudomorphs after sulphates. Meniscus and pendular cements, keystone vugs, desiccation cracks are present. Beds are sometimes lenticular.
S2	This cycle is the most common, with thickness from a few cm to 7 m. It is a homogeneous mudstone overlain by an intraformational conglomerate, laminar detrital mudstone and topped by stratiform stromatolites, brecciated or not. Desiccation cracks, vadose cements, pseudomorphs of evaporative crystals are common. Beds are lenticular or not.
S1	Thickness varies from 0.8 m to 5 m with variable internal composition. The cycle is a succession of ooid grainstone/packstone, floatstone/packstone with abundant aggregates, peloidal grainstone/packstone, intraformational conglomerate, laminar detrital mudstone topped by stratiform stromatolites. Vadose cementation occurs. Beds must be lenticular.
D2	The cycle varies from 2 m to 10 m. The base of the cycle is a biohermal stromatolite (> 1 m) overlain by ooid grainstone/packstone or homogeneous mudstone, intraformational conglomerate, laminar detrital and by stratiform stromatolites in the top. Stromatolites show no evidence of exposure.
D1	The thickness ranges from 4 m to 20 m. The cycle is characterized by purplish laminar clayey and silty mudstones topped by giant stromatolites with no evidence of subaerial exposure.

Type	Cycle features
S3	This cycle is relatively rare and less than 1.5 m-thick. The succession consists of pisoidic grainstone/floatstone, intraformational conglomerate, laminar detrital mudstone overlain by laminar microbial mats and evaporitive mudstone with abundant pseudomorphs after sulphates. Meniscus and pendular cements, keystone vugs, desiccation cracks are present. Beds are sometimes lenticular.
S2	This cycle is the most common, with thickness from a few cm to 7 m. It is a homogeneous mudstone overlain by an intraformational conglomerate, laminar detrital mudstone and topped by stratiform stromatolites, brecciated or not. Desiccation cracks, vadose cements, pseudomorphs of evaporative crystals are common. Beds are lenticular or not.
S1	Thickness varies from 0.8 m to 5 m with variable internal composition. The cycle is a succession of ooid grainstone/packstone, floatstone/packstone with abundant aggregates, peloidal grainstone/packstone, intraformational conglomerate, laminar detrital mudstone topped by stratiform stromatolites. Vadose cementation occurs. Beds must be lenticular.
D2	The cycle varies from 2 m to 10 m. The base of the cycle is a biohermal stromatolite (> 1 m) overlain by ooid grainstone/packstone or homogeneous mudstone, intraformational conglomerate, laminar detrital and by stratiform stromatolites in the top. Stromatolites show no evidence of exposure.
D1	The thickness ranges from 4 m to 20 m. The cycle is characterized by purplish laminar clayey and silty mudstones topped by giant stromatolites with no evidence of subaerial exposure.

### **Saris section**

The Saris section (Fig. 14) shows well-developed S2 cycles in the lower part with dominant S1 cycles in the upper part. It consists of 11 meter- to plurimeter-scale cycles with a pronounced thickening-upward trend at the fourth-order. The mean thickness is 0.85 m for the S2 cycles (ranging from 0.4-1.3 m) and is 6.5 m (ranging from 3.0-11.5 m) for the S1 cycles.

Two parasequences sets are present, the first one with S2 cycles is aggradational and the second one with S1 cycles is strongly progradational.

### **D section**

The D section (Fig. 15) shows dominated S2 parasequences overlain by open marine D1 parasequences. It is composed of centimeter- to meter-scale facies assemblages with 73 elementary S2 parasequences and, in its upper part two plurimetric D1.

Four parasequence sets are recognized (i) aggradational 1 (minimum 4.2 m-thick) with very thin S2 cycles without thickness evolution, (ii) progradational 2 (at least 10.8 m-thick with 5 metric S2 cycles, averaging 2.2 m and ranging from 0.6-4 m), (iii) aggradational 3 with at least six S2 cycles (9.9 m-thick, averaging 1.7 m) without clear thickness evolution, (iii) aggradational 3 (at least 6.3 m-thick) and (iv) progradational 4 ( $\pm$  25 m-thick) with at least two D1 cycles showing a pronounced thickening-upward evolution.

## Highlights

1. The SC<sub>1c</sub> Formation records the evolution of a marine ramp
2. It is a carbonate succession of meter-scale shallowing-upward cycles
3. The cycles are the result of the interplay of relative sea-level changes
4. The SC<sub>1c</sub> cycles are enclosed into a third-order sequence related to the deposition of the SCI

Subgroup

Journal Pre-proof

**Declaration of interests**

The authors declare that they have no known competing financial interests or personal relationships that could have appeared to influence the work reported in this paper.

The authors declare the following financial interests/personal relationships which may be considered as potential competing interests: